International Journal of Solids and Structures 279 (2023) 112389

Contents lists available at ScienceDirect

International Journal of Solids and Structures

journal homepage: www.elsevier.com/locate/ijsolstr

Impact response of negative stiffness curved-beam-architected metastructures

Navid Mehreganian [a], Arash S. Fallah [b], Pooya Sareh [a,*]

[a] Creative Design Engineering Lab (Cdel), Department of Mechanical and Aerospace Engineering, School of Engineering, University of Liverpool, Liverpool L69 3GH, United Kingdom
[b] Department of Mechanical, Electronic, and Chemical Engineering, OsloMet, Pilestredet 35, St. Olavs plass, Oslo 0166, Norway

ARTICLE INFO

Keywords:
Mechanical metamaterials
Negative stiffness honeycomb metastructure (NSHM)
Bistability ratio
Snap-through buckling
Poincaré-Lindstedt method

ABSTRACT

Mechanical metamaterials and metastructures exhibit superior effective mechanical properties, such as enhanced energy dissipation and resistance against impact loads, beyond those of natural materials. Metastructures with the ability to manipulate wave propagation are particularly desirable in numerous applications, such as actuators, dampers, and lightweight impact resistant systems with structural tunability and recoverability. Specifically, multi-stable structural forms have attracted considerable attention in the design of architected multi-materials, metamaterials, and morphing structures. To design such systems, a recently developed mechanical metamaterial/metastructure known as negative stiffness honeycomb, composed of arrays of curved double-beams (CDBs), is proposed. Here, we develop an analytical model to predict the dynamic response of the CDB metastructures, architected with a periodic array of the CDBs, and subjected to impact by a striker. The analytical model is developed using the Euler-Lagrange theorem and the snap-buckling phenomena in the honeycomb have been examined. The derived closed-form solutions were in good agreement with those of the numerical finite element model at different bistability ratios, defined as the ratio of beam apex height to its thickness. The findings demonstrated that the bistability ratio had a noticeable influence on the buckling response of the metastructure and the desired negativity in the stiffness matrix, while the snap-back buckling phenomena may be realised at high bistability ratios.

1. Introduction

The terms ‘metamaterial’ and ‘metastructure’, used interchangeably at times, refer to a broad class of structured materials and composites that can be tailored to have desired subwavelength characteristics not readily found in natural materials. The properties of metamaterials and metastructures stem from characteristics that pertain to their constituting unit cells rather than atomic or molecular micro- or nano-structures. Auxetic, chiral, acoustic, labyrinthine, and phononic are classes of metamaterials, to name a few. In an acoustic metamaterial, for instance, the resonant frequency of the cells depends on their inertia and restoring force (stiffness) thus the relevant wavelength at the resonant frequency of the unit cell is of an order larger than its dimensions (Kochmann and Bertoldi, 2017; Ma and Sheng, 2016). Dependence of features on unit cell properties results in manifesting controllable characteristics such as in wave dispersion giving rise to functionalities such as chirality (Lakes, 2001; Frenzel et al., 2017), negative Poisson’s ratio (Wu et al., 2019; Zheng et al., 2021), doubly-negative metamaterial of effective mass density and bulk modulus (Brunet et al., 2015), and energy entrapment (Shan, 2015) due to negative stiffness. These properties are related to classes such as auxetic (i.e. having negative Poisson’s ratio) (Baughman, 2003; Alderson and Alderson, 2007; Chen et al., 2021, 2022; Jalali et al., 2022; Sareh and Guest, 2014, 2015a, 2015b, 2015c; Lu et al., 2024), single- and multiple-resonator acoustic/phononic (Fallah et al., 2015; Gorshkov et al., 2017; Gorshkov et al., 2021, 2023) (i.e. having negative effective mass density), and negative stiffness mechanical metamaterials (Fang et al., 2006; Lakes et al., 2001). Features like negative Poisson’s ratio and negative stiffness bring about enhanced toughness, improved in-plane transverse shear resistance, and augmented impact energy absorption and wave guiding, while negative stiffness establishes an essential feature of the multi-stable structural elements. Although the theoretical foundations for achieving these features have existed for a long time, the realisation is rather recent.

The advent of advanced additive manufacturing technologies,

* Corresponding author.
E-mail address: pooya.sareh@liverpool.ac.uk (P. Sareh).

https://doi.org/10.1016/j.ijsolstr.2023.112389
Received 8 August 2022; Received in revised form 15 May 2023; Accepted 12 June 2023
Available online 15 June 2023

Nomenclature

Latin upper-case

$A_{j,i}$	Displacement field amplitude of the j^{th} odd modes for the i^{th} curved beam; [1]
$A_{k,i}$	Displacement field amplitude of the k^{th} even modes for the i^{th} curved beam; [1]
A	Closed surface Area; [m^2]
C_i	Integration coefficients; [1]
E	Young's Modulus; [Pa]
G	Mass of the striker; [kg]
I	Second moment of area; [m^2]
L_x	Characteristic length of the structure; [m]
M	Bending moment per unit length; [N]
N_x	Membrane force per unit length; [N/m]
P	Transverse load; [N]
$\overline{P}$	Dimensionless transverse load; [N]
P_t	Reaction force at boundaries; [N]
T	Kinetic energy; [J]
T_s	Kinetic energy of the struts; [J]
T_b	Kinetic energy of the curved beam; [J]
T_{st}	Kinetic energy of the striker; [J]
U_b	Bending strain energy; [J]
U_m	Membrane strain energy; [J]
U_s	Elastic potential energy; [J]
V	Striker velocity; [m/s]
V_0	Velocity of the striker at the onset of impact; [m/s]
$\mathscr{W}$	External work done; [J]
W_0	Original configuration of the curved beam; [m]

Latin lower-case

$a_i - b_i$	Displacement coefficient; [1]
b	Beam width; [m]
d	Deformation of mid-span; [m]
$\widehat{f}(x,y,t)$	Pressure load; [Pa]
h	Rise of the curved beam; [m]
$\overline{h}$	Bistability ratio; [1]
k_i	Stiffness of the i^{th} member; [N/m]
l_0	Beam span; [m]
m	Mass of the lattice struts and buckled beams; [kg]
$m_{b,i}$	Inertia mass of the i^{th} curved beam; [kg]
p_s	Scaled dimensionless load; [1]
p	Membrane force; [N]
s	Length of the curved beam after deformation; [m]
s_0	Initial length of the curved beam; [m]
$t_{d,i}$	Duration of the i^{th} phase; [s]
t^*	Time scale for mass of the lattice; [s]
t_1^*	Time scale for mass of the curved beam; [s]
w_j	Displacement field of the odd modes; [1]
w_k	Displacement field of the even modes; [1]

Greek upper- and lower-case

Δ	Dimensionless mid-point displacement of the curved beam; [m]
Δ_t	Total dimensionless displacement of the structure; [m]
ϵ_0	Perturbation parameter; [1]
κ	Curvature; [m^{-1}]
μ	Mass per unit area; [kg/m^2]
μ_s	Mass per unit area of the beam; [kg/m^2]
ρ_b	Beam density; [kg/m^3]
$\widehat{\tau}$	Section thickness; [m]
τ	Scaled time; [1]
τ_{cb}	Horizontal stiffeners thickness; [m]
ψ	Membrane Stiffness coefficient; [s^{-2}]
λ	Perturbed vibration frequency of the beam; [Hz]
λ_0	Vibration frequency of the beam; [Hz]
λ_1	First vibration pseudo frequency of the beam; [Hz]
λ_2	Second vibration pseudo frequency of the beam; [Hz]
ω_0	Eigenvalues; [1]
ω_j	Modal frequencies of the j^{th} mode; [1]
ω_k	Modal frequencies of the k^{th} mode; [1]

recently developed and commonly employed to fabricate multifunctional structural frameworks of complex internal microstructures, has made it possible to create physical models of designs with desired features such as bistability/multi-stability. The development of such multistable structural forms, alongside a better understanding of fundamental nonlinear theories of continuum mechanics (Truesdell and Toupin, 1960; Toupin, 2013; Truesdell, 1968; Yavari et al., 2000; Yavari, 2008), has facilitated the fabrication of lightweight, impact-resistant structures with high load-bearing capacity composed of slender structural elements. These adaptive forms undergo shape change while providing appreciably high strength, thus offering a basis for the design of morphing structures. To this end, various methods exist to render multistability in structural elements feasible, such as through applying prestress (Daynes et al., 2008; Fulcher et al., 2014), introducing thermal effects (Jeong et al., 2019; Chen et al., 2023), or initial curvature (Street and Seffen, 2007; Chen et al., 2023). In this regard, Vangbo (Vangbo, 1998) and Qiu and Lang (Qiu, 2003; Qiu et al., 2004) proposed an analytical model for mechanically-bistable curved beams with a prefabricated geometric profile, similar to that of a conventional beam, which is deformed into the first Euler's buckling mode when subjected to an external concentrated force (actuation) at its mid-span. Analytical investigations were validated by microscale experimental models using an actuator. Cazottes et al. (Cazottes et al., 2009) studied the same problem for a curved single-beam (CSB) with the force applied at different locations. Camescasse (Camescasse et al., 2013) investigated the static actuation of an arch with initial constant curvature. They discussed that for the reduced two degree-of-freedom model, the equilibrium path in the transition from one stable equilibrium position to another follows an unstable region of bistable energy. Other experimental studies on the CSB (Restrepo et al., 2015) and bistable CDB composites made of individual or bi-materials (Chen, 2020) investigated the bistability of the lattices under static loading conditions.

Being no longer a tantalizing dream, microstructured materials with multi-stable states were printed to serve a variety of applications. Mechanical systems that exhibit bistability are ideal candidates for applications in areas such as autonomous systems and robotics (Sareh et al., 2018; Mooney and Johnson, 2013; Alonso-Mora et al., 2015; Chen et al., 2023) as well as product design (Lv et al., 2014; Sareh, 2019; Liu et al., 2019). Experimental evidence has demonstrated that the desired bistability in the CDBs provides two distinct stable positions. A mode transition that occurs in the buckled beam from one stable position to another is accompanied by the reduction of the force level which results in the release of the stored strain energy (Cazottes et al., 2009; Camescasse et al., 2013). This contributes to the tunability of such systems.

Many composites are deemed untunable, meaning that their dynamic properties cannot be altered without changing the microstructure. In metamaterials of negative stiffness, tunable wave propagation is often achieved by constructing a periodic lattice of the constituent cells i.e., tessellating the unit cell incorporating bistable beams whereby the periodic boundary conditions and Bloch-Floquet principle may be used.

This is not the only way to achieve tunability in a composite as tunability in a heterogeneous medium may also be achieved through the introduction of random inclusions. For example, Konarski (Konarski et al., 2020) developed a multi-scale material model with randomly dispersed spherical negative stiffness inclusions for the dynamic behaviour of the matrix material against acoustic perturbations. Brunet et al. (Brunet et al., 2015) designed a new class of 3D negative acoustic index non-periodic metamaterial made of porous soft silicon rubbers, in which the negative acoustic index emanates from the low-frequency resonances of sub-wavelength particles.

Due to the desired recoverability and potential tunability, bistable beam structures could be integrated into mechanical systems that, sequentially, store and release energy elastically, with little or no energy dissipated plastically thus no damage incurred. Such properties provide resilience and robustness against repeated impacts, enabling them to recover from an initial impact and respond to subsequent impacts, hence increasing the life cycle of the structure. Under the circumstances of repeated impacts, the transverse displacement of the structural element approaches that which would have occurred if a load of equal magnitude had been exerted statically, a phenomenon referred to as the pseudo-shakedown (Jones, 2014). Examples of recoverable systems are the recently fabricated negative stiffness honeycomb metastructures (NSHM) which, when subjected to lateral unidirectional loads, exhibit close to zero Poisson's ratio and negative stiffness as the most important attributes (Correa et al., 2015). NSHM refers to a decrease in the load magnitude following a jump in the displacement field of the honeycomb structure. While the response of the NSHM cells, as investigated by (Correa et al., 2015), was found to be similar to the hexagonal honeycomb structure, the NSHM lattice featured considerably higher recoverability (i.e. negligible plastic deformation) compared to its conventional hexagonal honeycomb counterparts. Under the circumstances where frequent collisions are inevitable, a structure made of these cells can be a viable choice.

The ability to modulate the material properties of a medium in time and space breaks parity-time symmetry, enabling non-reciprocal elastic wave phenomena (Goldsberry and Haberman, 2018). Examining the tunability of the NSHM made of the CDBs, the authors of (Goldsberry and Haberman, 2018) sought the Bloch wave solutions in the NSHM subjected to an affine, uniaxial macroscopic pre-strain values of $\beta =$ 0, 0.0101, 0.0207, and 0.0252, whereby the prescribed macroscopic deformation gradient $F_{ij} = u_{i,j} + \delta_{ij}$ (with δ_{ij} being the Kronecker delta) was expressed as $F = \begin{bmatrix} 1 & 0 \\ 0 & 1-\beta \end{bmatrix}$, and showed that the size and extrema of the bandgap frequencies range decreased with the increase in pre-strain. Pre-strain below the point of instability in the NSHM lattice enables the tunability of bulk elastic wave propagation. Chen *et al.* (Chen, 2020) experimentally investigated the cyclic quasi-static and plate impact loading of the composite NS structural element, whereby the CDBs made of very soft material (Thermoplastic Polyurethane) were compounded with Polyamide bars. The former results revealed that the force threshold of the prototypes having a low thickness in the rigid elements was reduced by less than 5% after 10 cycles, offering high recoverability of the composite element. Furthermore, the compressive strength of the NSHM lattice made of two cells was higher than the combined compressive strength of the single-material negative stiffness structure. Considering the plate impact tests, the acceleration threshold causing the full compression was significantly amplified with the increase of the impactor height beyond 0.45 m. Meaud (Meaud, 2018) examined the elastic wave propagation in a two-dimensional periodic lattice including alternative patterns of linear and nonlinear bistable springs.

From the load–displacement viewpoint, the snap-through instability phenomenon is associated with the sudden jump in the displacement in the load-control curve. A counterpart phenomenon referred to as the snap-back, however, occurs in the displacement-control curve when the load reduces suddenly even without an increase in the prescribed displacement (Sun et al., 2019). The curved beam profile undergoing snap-back reverses from bulge down to bulge up. In the lattice made of multiple arrangements of the bistable beams in a modular pattern, the force landscape of the snap-buckling chain mechanisms exhibits erratic curves, altering between various equilibrium states leading to the evolution of the energy entrapment. Subsequently, the lattice exhibits hysteresis upon loading–unloading cycles.

Researchers (Sun et al., 2019; Rafsanjani et al., 2015) examined the instability of an RVE (representative volume element) mechanical system comprising two or more cosine-shaped, curved beams paired vertically in series, wherein the top beam was thinner than the bottom one. The hysteresis of the structure was examined under displacement-control loading whereupon its difference with the load-control loading was elucidated. Upon stretching at the edges, the curvature of the top slim beam changed while that of the bottom beam remained relatively constant. For a lattice made of such an RVE, wherein the middle beams were shorter than the top and bottom ones, curvature reversing was observed in both the middle shorter beams and the top, thick, longer beam, while the shape of the bottom beam remained unchanged in the various loading scenarios. In a similar study (Chen and Jin, 2020), the snap-back phenomenon was observed in the thick hyperelastic columns where both force and displacement levels were reduced after the onset of loading.

Recently, there has been a resurgence of interest in the structural mechanics of honeycomb structures, owing, not only to their superior relative high stiffness and strength but also to efficient specific energy absorption during accidental impacts (Gibson and Ashby, 2001; Tancogne-Dejean et al., 2016). These structures feature a large constant plateau in their stress-deformation path between the initial yield and a densification phase. Although the relative density is a prime factor (Tancogne-Dejean et al., 2016; Gibson and Ashby, 1997; Hu et al., 2018) in the mechanical performance of honeycombs, other factors such as cell wall angle, loading conditions, cell structure, and geometry also play important roles. For instance, hexagonal honeycomb structures subjected to compressive loading exhibit different buckling modes depending on the loading condition. In uniaxial compression, two kinds of cell collapse appear and alternate in the loading direction as a result of cell wall buckling, while in biaxial compression the buckled cell pattern entails two orthogonal axes of symmetry (Okumura et al., 2002).

A range of analytical (Okumura et al., 2002; Hu and Yu, 2010), experimental (Hou et al., 2012; Hou et al., 2011), and numerical (Hou et al., 2012; Zou et al., 2009) investigations have been carried out on the mechanical behaviour of hexagonal honeycomb structures. Zheng et al (Zheng et al., 2005) presented a finite element model for the dynamic crushing of hexagonal honeycomb structures. Hu et al. (Hu et al., 2013; Hu and Yu, 2013) investigated the same problem, experimentally as well as computationally, but with the influence of the cell wall angle and impact velocity on the crushing behaviour included. They showed that in the honeycombs experiencing high-velocity impacts, a localised crushing band occurs at the loading band normal to the impact direction, which propagates layer by layer to the supporting ends, while the honeycombs with increased cell wall angles, at impact velocities above 40 m/s, undergo deformation modes similar to that of high-velocity impacts, regardless of the initial impact velocity. By assuming the beam element behaviour for the members, Ouyang et al. (Ouyang et al., 2018) studied the stress concentration in defective octagonal honeycombs (with missing cell walls along a row) subject to uniaxial tension. They found that the stresses in the cell walls decrease exponentially with increasing distance from the centre of the defect.

Previous studies (Emam, 2002; Nayfeh and Emam, 2008) analysed the static post-buckling response and dynamic vibration of buckled clamped–clamped beams subject to harmonic excitations, theoretically and experimentally. Using the multi-mode Galerkin discretisation, the period-doubling bifurcation, snap-through, and quasi-periodic motions were examined. The effective nonlinearity, or the quotient of the

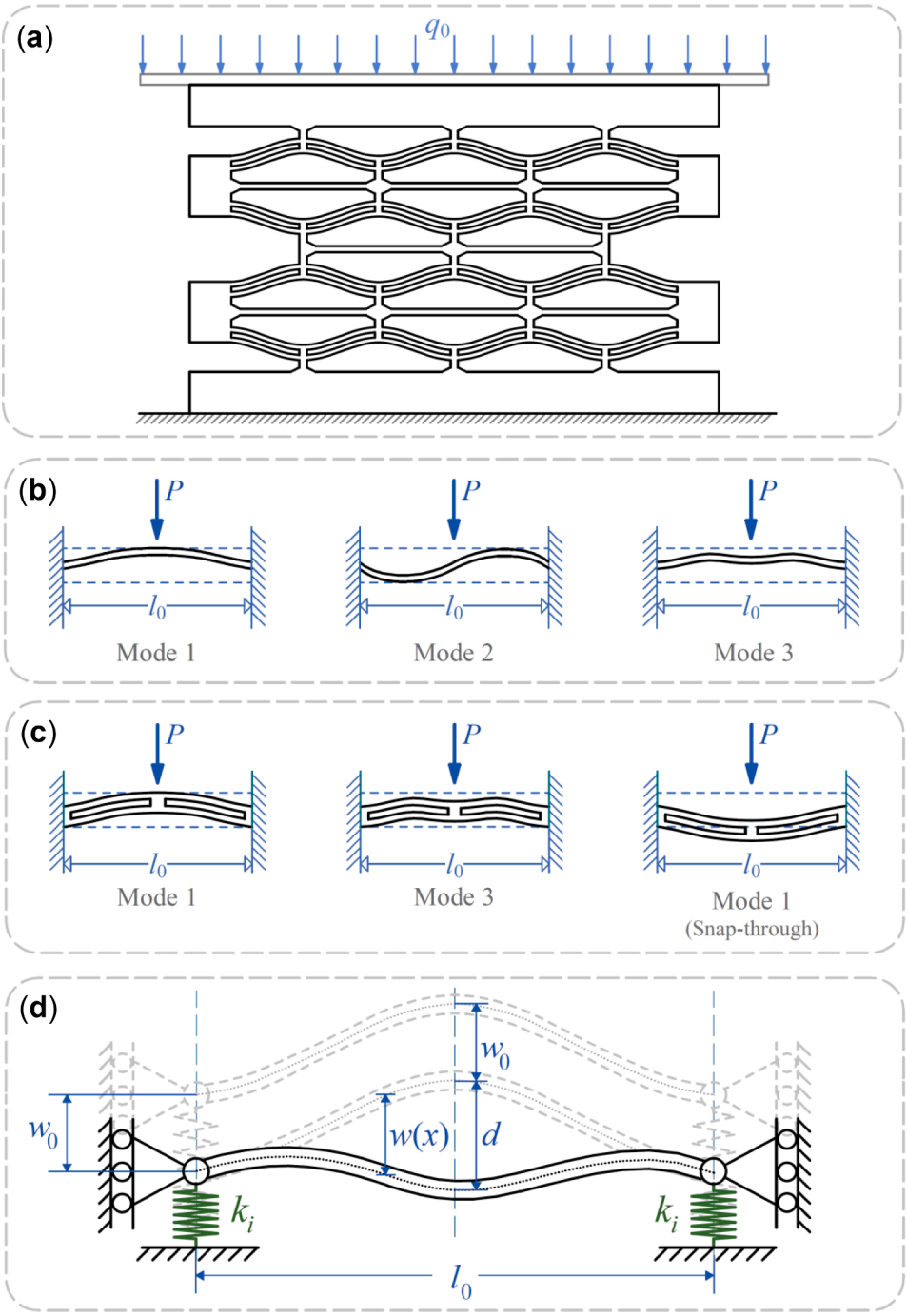

Fig. 1. (a) The schematics of NSHM composed of curved double-beams (CDBs) and straight stiffeners for analytical study. (b) Buckling modes of a curved single-beam (CSB) with axisymmetric boundary conditions. (c) Buckling modes of a CDB with a mid-point stiffener with axisymmetric boundary conditions. (d) Deformation of a CSB subjected to a concentrated transverse load (Mehreganian et al., 2021).

functional of displacement field over a closed surface to the vibrational frequency, remained negative below the critical buckling level (buckled displacement at mid-span). The latter work derived exact solutions to the post-buckling of the beams with different boundary conditions. Li et al. (Li et al., 2004) investigated the vibration of a thermally buckled beam with geometric nonlinear effects retained in the buckling and post-buckling analyses.

Despite the interesting studies mentioned above, research on the dynamic response of the NSHM is still in its infancy, given most studies have focused on conventional honeycombs as lattice structures subject to static loading. This work proposes an analytical model to delineate the impact resistance of the NSHM with potential application in the design of recoverable protective structural forms.

The dissemination of this paper is organised into five sections. Following this introduction, the fundamental mathematical expressions for the response of the bistable curved beam are developed. In Section 3, the equations of motion are derived using the extended Hamilton's principle and an analytical solution is sought for an impact-loaded honeycomb structure, which is designed from the modular pattern of the CDBs with guided supports (zero rotations and free translations), using perturbation techniques on the derived conservation of energy equations. Section 4 develops the numerical Finite Element models to

examine the validity of the analytical model. Finally, Section 5 presents the conclusions of the study.

2. Structural mechanics of the NSHM

The metastructure model assessed here, as depicted in Fig. 1a, is composed of a finite collection of constituent cells with two cells located in each column (along the direction of the load) and an arbitrary number in each row. Each cell is architected with two pairs of curved beams, interconnected via horizontal stiffeners and vertical struts. The model design is similar to that proposed previously by researchers in the field (Correa et al., 2015; Goldsberry and Haberman, 2018). The symmetry of the model reduces the mathematical treatment to consideration of only one cell along the horizontal direction (perpendicular to the loading direction) but includes all the curved beam pairs along the loading direction.

The structure is subject to an impact load by a striker of mass G and impact velocity V_0. It is assumed that the structure remains purely elastic throughout the motion. Nevertheless, the influence of finite displacements, or geometry changes, is retained in the analyses, which gives rise to the evolution of the membrane (catenary) forces. The so-emerged membrane forces resist out-of-plane deformation and alleviate its maximum displacement at the expense of higher in-plane stresses (Mehreganian et al., 2018).

The so-fabricated curved beams have a sinusoidal profile that mimics a monolithic Euler-Bernouli beam buckled into its first Euler buckling mode (see Fig. 1b). Upon the application of the load, the curved beam pairs (CDBs) exhibit bistability (Qiu et al., 2004), i.e., they jump abruptly from mode 1 to 3 without undergoing mode 2 (see Fig. 1c). The bistability condition can be satisfied when the bistability ratio $\bar{h}$ is large enough ($\bar{h} > 2$) and the curved beams are made into a pair by clamping at the centre (Qiu et al., 2004; Mehreganian et al., 2021). Therefore, the deformation of the CDBs may be assumed to be homogeneous with no relative displacements between the curved beams in the CDB. Furthermore, the pairing of the beams ensures that mode 2 is constrained and subsequently the influence of this mode can be ignored in the theoretical analyses.

Under static loading, the deformation of the NSHM model, according to the experimental and numerical evidence (Correa et al., 2015), may be broken down into four distinct stages, namely (i) snap-through buckling of the upright beams at the top layer, (ii) downward movement of the struts, while, simultaneously, the CDBs underneath the corresponding strut undergo transverse deformation, (iii) snap-through in the inverted beams of the upper row, and (iv) snap-through buckling of the upright CDBs in the bottom layer which is accompanied by full compression of the structure. At each stage throughout the motion, the kinematic admissibility of the displacement field and the stress state are ensured so that there are no 'jumps' in the deformation.

It is straightforward to show that the original configuration of a curved beam fixed at each end must have the first Euler's buckling mode profile, expressible as (Qiu et al., 2004):

$$W_0 = \frac{h}{2}\left(1 - \cos\left(\frac{2\pi x}{l_0}\right)\right), \tag{1}$$

where h and l_0 are the rise and the initial length of the beam, respectively. Such a profile is a condition that can satisfy the bistability criterion. The respective profiles of the beam in its original and deformed configurations are illustrated in Fig. 1d.

The structural system may be regarded as a discrete, purely elastic system of n degrees of freedom representative of the deformations of the CDBs. Following (Qiu et al., 2004), the displacement field of the curved beam w is decomposed into a linear combination of modal displacements, i.e. $w = \sum_j w_j + \sum_k w_k$, each component of which, upon using the mode superposition method, is expressible as:

$$w_j = hA_j\left(1 - cos\left(\frac{\omega_j x}{l_0}\right)\right) \tag{2}$$

for the modal frequencies of $\omega_j = 2n\pi$ where $j = 2n-1$, with n being an integer representing the mode number of the displacement profile, and

$$w_k = hA_k\left(1 - \frac{2x}{l_0} - \cos\left(\frac{\omega_k x}{l_0}\right) + \frac{2\sin\left(\frac{\omega_k x}{l_0}\right)}{\omega_k}\right), \tag{3}$$

where $\omega_k = 2.86\pi, 4.95\pi, \cdots$ for mode numbers $k = 2, 4, 6, \cdots$. The modal frequencies of even subscripts are calculated from the solution to the axial compression of a clamped straight beam to a stable position, i.e., the condition $\tan(\omega_k/2) = \omega_k/2$. Thus, $w = \sum_{n=1}^{\infty} A_j\left(1 - cos\left(\frac{\omega_j x}{l_0}\right)\right)$.

Such a curved beam with the profile of Eq. (2) is paired in each cell and restrained with roller boundary conditions whereby only transverse deformations are permissible throughout the motion, the CDB pair constrain rotations that would otherwise admit asymmetric modes from the solution, as the centre clamp transfers the rotational degree of freedom of either beam centre to an axial DOF of the lower beam.

Interestingly, the consequence of pairing the curved beams is to disregard the mode shapes of even numbers in the mathematical analysis, hence simplifying the analysis significantly with consideration of Eq. (2) as the basis of the buckling response of the NSHM due to impact. Upon loading, the lateral displacement at the mid-span of the beam becomes $d = W_0(l_0/2) - w(l_0/2)$. Subsequently, the expression for bending and membrane strain energies, U_b and U_m are, respectively, given by:

$$U_b = \frac{EI}{2}\int_0^{l_0}\left(\frac{\partial^2 W_0}{\partial x^2} - \frac{\partial^2 w}{\partial x^2}\right)^2 dx, \tag{4}$$

$$U_m = -\int_0^{l_0} p ds, \tag{5}$$

where the parameter s represents the arc length i.e., the new length of the curved beam upon deformation. To evaluate Eq. (5), by using the moderate deformations approximation $ds = dx\sqrt{1 + \left(\frac{dw}{dx}\right)^2} \cong dx\left(1 + \frac{1}{2}\left(\frac{dw}{dx}\right)^2\right)$, we have:

$$s = \int_0^{l_0}\left(1 + \frac{1}{2}\left(\frac{dw}{dx}\right)^2\right)dx. \tag{6}$$

The initial length of the beam, i.e. $s_0 = (\pi^2 h^2 + 4l_0^2)/(4l_0)$, is obtained by replacing w with W_0 in Eq. (6). The membrane force induced by the change of beam length is determined as

$$p = Eb\hat{\tau}\left(1 - \frac{s}{s_0}\right). \tag{7}$$

Eqs. (2), (4)-(7) construct the basis for the mathematical procedure to verify the buckling response of the CDB. The relative displacements between the vertical struts and the curved beams are assumed negligible by postulating that they behave as inextensible struts. Furthermore, it is assumed that the horizontal stiffeners remain undeformed during the deformation. The presence of the horizontal stiffeners causes the CDB pairs to be tied on either side and to eliminate the lateral deformations in the system, thus rendering the deformations homogeneous. The downward motion of the NSHM structure is thus solely associated with the local snap-through (snap-back) of the curved beam pairs in each layer. Based on the research by (Qiu et al., 2004; Correa et al., 2015; Nayfeh and Emam, 2008) and/or by applying Buckingham's Π-theorem, a dimensionless set of parameters can be derived as follows:

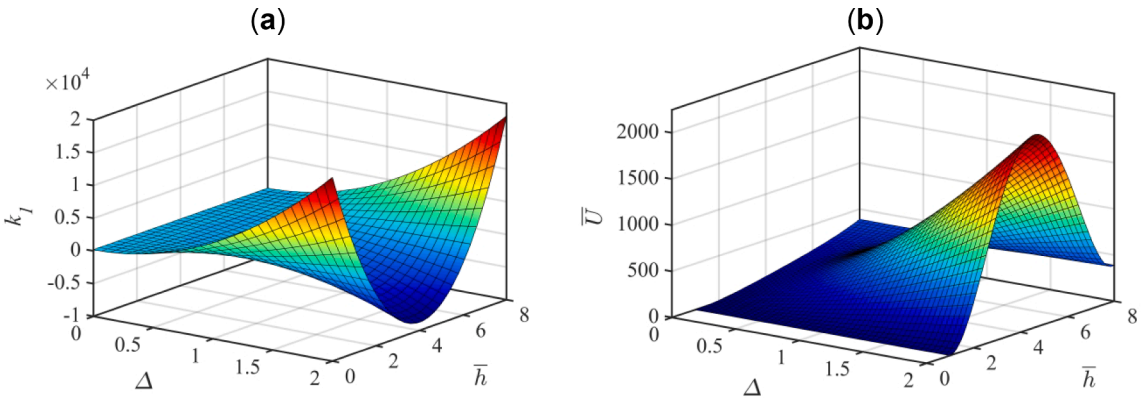

Fig. 2. (**a**) Interaction of the bistability and deformation on the beam tangent stiffness. (**b**) Influence of the beam bistability ratio on the elastic strain energy of the beam expressed as $\bar{U} = \int \bar{P} d\Delta$, derived from Eq. (15).

$$\bar{w}_j = \frac{w_j}{h},\ \bar{l} = \frac{l_0}{h},\ \bar{h} = \frac{h}{\tilde{\tau}},\ \bar{U}_b = \frac{U_b l_0^3}{EIh^2},\ \bar{U}_m = \frac{U_m l_0^3}{EIh^2},\ \bar{P} = \frac{Pl_0^3}{EIh},\ \bar{x} = \frac{x}{l_0},\ \Delta = \frac{d}{h},\ \bar{s} = \frac{sl_0}{h^2},\ \text{and}\ \bar{p} = \frac{pl_0^2}{EI}. \tag{8a-j}$$

The parameter $\bar{h}$ in Eq. (8b), developed by Qiu et al. (Qiu et al., 2004) and later adopted and used by others as Correa et al. (Correa et al., 2015), represents the bistability ratio which permits a rational comparison between the amount of stored energy due to the deflections of different lattices to be made. It must be appreciated that although the elements in the set of dimensionless parameters may take different forms, the cardinality of the set of these parameters is unique. The relative significance of various dimensionless parameters may be found by other means (Li and Jones, 2000). Here, because of the importance of beam characteristic lengths, in particular, the beam apex height and thickness, the non-dimensional expressions for structural strength, stiffness, strain energies, and force, have been related to these parameters.

Substituting Eqs. (8) Eqs. (4)-(7), the dimensionless parameters of Eqs. (8a-j) are calculated as:

$$\Delta = 1 - 2\sum_{j=1,5,9,..} A_j, \tag{9}$$

$$\bar{s} = \left(\bar{l}^2 + \sum\nolimits_{j=1}^{\infty} \frac{\omega_j^2 A_j^2}{4}\right), \tag{10}$$

$$\bar{p} = \frac{3\bar{h}^2}{\bar{s}_1}\left(\frac{\omega_1^2}{4} - \sum\nolimits_{j=1}^{\infty} \omega_j^2 A_j^2\right), \tag{11}$$

$$\text{where } \bar{s}_1 = \omega_1^2/16\bar{l}^2 + 1 = s_0/l_0. \tag{12}$$

It is assumed that the as-fabricated curved beam is stress-free at $\Delta = 0$; therefore, the leading-order terms of Eqs. (4)-(5) are expressed, respectively, as:

$$\bar{U}_b = \frac{\omega_1^4}{4}\left(\frac{1}{2} - A_1\right)^2 + \sum\nolimits_{j=2}^{\infty} \frac{\omega_j^4 A_j^2}{4}, \tag{13}$$

$$\bar{U}_m = \frac{12l_0^2}{\tilde{\tau}^2}\left(\bar{s} - \frac{8\bar{s}^2}{\omega_1^2 + 16\bar{l}^2}\right). \tag{14}$$

The expressions above establish the fundamental ingredients for solving the problem of curved beam buckling in the case of static loading. By utilising the Lagrange-Dirichlet theorem, the total potential energy Π which corresponds to the strain energies and the work done, considering every mode of deformation, is stable and has a strict minimum (Bazant and Cedolin, 2010; Szilard, 2004; Wadee et al., 2020). Furthermore, the equilibrium expression of the system can be derived from the stationarity condition of the system. In the case of dynamic loading, however, the kinetic energy (corresponding to inertia force terms) must also be included in the formulation of the total energy Π. For a single beam, it can be demonstrated that the force–displacement and stiffness of the beam obey the following relations (Mehreganian et al., 2021)

$$\bar{P} = \frac{\pi^4 \Delta\left(\left(12(\Delta-1)(\Delta-2)\bar{h}^2 + 16\right) + 4\pi^2/\bar{l}^2\right)}{8\bar{s}_1}, \tag{15}$$

$$k_1 = \frac{\left(\left(4 + 3(3\Delta^2 - 6\Delta + 2)\bar{h}^2\right)\bar{l}^2 + \pi^2\right)\pi^4}{2\bar{l}^2\bar{s}_1}. \tag{16}$$

Fig. 2 illustrates the influence of the bistability ratio $\bar{h}$ and the transverse displacement of the single curved beam on its tangent stiffness (Eq. (16)).

For convenience, further dimensionless numbers are introduced as follows.

$$t^{*2} = \frac{ml_0^3}{EI},\ t_1^{*2} = \frac{m_b l_0^3}{EI},\ \bar{G} = \frac{G}{m},\ \bar{T} = \frac{Tl_0^3}{EIh^2},\ \bar{g} = \frac{g}{h},\ \dot{\bar{W}}_{(i)} = \frac{\dot{W}_{(i)}}{h},\ \bar{m} = \frac{m_b}{m}. \tag{17a-h}$$

The dynamic response of the NSHM during the impact loading consists of the n main phases of motion, as expounded in detail in the sequel, where n represents the number of CDBs in the direction of the load.

3. Striker impact on the NSHM

This section deals with the analyses of the dynamic response in the NSHM due to the impact of a striker of a particular mass and geometry. The type of contact is assumed to be hard contact (normal behaviour) with penalty frictional formulation (tangential behaviour). In the following subsections, the distinct phases of motion are analysed in detail.

A considerable body of literature exists on the dynamic response of plate and beam elements subjected to impact by a heavy mass striker (Jones, 2014; Johnson et al., 2009; Dean et al., 2011; Jones, 2012). For simplicity in the mathematical treatments, the material behaviour of such structural elements is, however, assumed to be either linear elastic or rigid-perfectly plastic (Mehreganian et al., 2018; Jones, 1989; Mehreganian et al., 2018; Jones, 2014). More often than not, the buckling of the structural members admits large displacements in which case the influence of finite displacements or geometry changes is non-negligible and nonlinear elastic analysis is required.

Before proceeding to the impact analysis of the NSHM, it is noteworthy to consider an arbitrarily shaped surface element bounded by an oriented closed path in the Cartesian coordinate system. Using Green's

theorem, the equation of motion in its force vector field is converted into a functional of energy conservation, wherein the total internal energy rate $\dot{\mathscr{D}}$ is at equilibrium with the external work rate $\dot{\mathscr{E}}$. As is customary, the overdot notation accounts for differentiation with respect to time. For an arbitrarily shaped plate (and a beam as a special case) when the shear strain and rotatory inertia effects are disregarded (Jones, 1989; Jones, 1971; Jones and Walters, 1983), we have:

$$-G\dot{V}\,V-\int_A \mu w^{\cdot}\dot{w}dA+\int_A \widehat{f}(x,y,t)\dot{w}d\overline{A}=\int_A (M+N_x w)\dot{\kappa}\,d\mathrm{A_c}, \tag{18}$$

where N_x is the membrane force per unit length, and $\dot{w}$ and V represent the velocities of the surface element and the striker, respectively. The expression on the left-hand side signifies the external work rate with the first term being the rate of change in the kinetic energy of the striker, and with the second and third terms giving the work due to pressure field $\widehat{f}(x,y,t)$ according to the Lagrange-D'Alembert principle's inertia force. The expression on the right-hand side gives the strain energy rate in the continuous deformation fields due to bending and membrane actions, respectively. Eq. (1) reduces to the equilibrium equation for Euler-Bernoulli beams by considering the variation in the generalized coordinate y to be negligible.

Given the impact duration is of the order much less than the natural period of the structure, the influence of viscoelasticity can be disregarded. Thus, the motion unequivocally resembles the forced vibration of a system comprised of linear springs (horizontal stiffeners) and nonlinear bistable springs (CDBs) interconnected in a given topology. The viscoelastic forces alter the constitutive equations, inducing mode coupling in the formulation of the lattice energy balance equations. Furthermore, as the CDBs in the lattice are slender, the effects of shear deformations and rotatory inertia are negligible.

3.1. First phase of motion $(0 \le t \le t_{d,1})$

Upon impact, the striker exerts a force on the top surface of the lattice at $t = 0$ and remains in contact with it for a duration of $t_d = t_{d,1}$, as the striker travels with the same velocity as the structure at the point of contact. Contrary to the buckling order in the static analysis, it turns out that the buckling of the CDBs initiates with the uppermost beams in the first (top) layer at the onset of impact loading. Subsequently, the CDBs buckle sequentially in order from the top to the bottom layer. Due to the geometry of the model, the induced axial deformation of the struts in each layer is associated with the buckling of the upright/inverted CDBs in the retrospective lattice column. The ensuing mathematical analysis may be pursued in two cases, namely: (*i*) the sequential buckling of the beams leading to the partial or full compression of the NSHM, or (*ii*) the response of the structure being brought about by the simultaneous buckling of the CDBs. From the numerical observations of the moderate velocity impacts considered, it transpires that the deformation of the lattice was driven by the dynamic buckling of the CDBs at each stage, while the simultaneous vibrations of the CDBs in the other layers were comparatively insignificant. Thus, in this work, we examine the first case scenario which, while offering simplicity to the mathematical treatment, preserves the accuracy of the solution.

With the mode-2 deformations and rotational degrees of freedom (DoFs) at each end of the CDB being constrained, the velocity profile of each would become independent of the other. Under such a circumstance, the governing equations of the multi-DoF system having n general modes of vibrations boil down to those of n single-DoF systems. The buckling of the i^{th} beam lasts for a duration of $t_{d,i}$ from the time point of $t_{d,\,i-1}$. At the point of transition in time between the buckling of each beam with the next one, the kinematic conditions of the velocity and displacement fields apply.

It may be assumed that the vertical bars behave as rigid bodies with no axial elongation/compression during the motion. An idealisation of the structure renders it to be visualised as a system of four lumped masses and springs connected by these bars. As the striker collides with the metastructure, the velocity of each lumped mass is equivalent to that of the mid-point of the CDBs.

Following D'Alembert's principle, as discussed earlier, and using Green's function on the principle of virtual velocities, the external forces (kinetic energy of the striker, inertia forces, and the work done by the striker) are equated, at every instant of time, to the total strain energy (bending and membrane) of the structure. The Lagrangian function Π is ensued, by enforcing a time integration of Eq. (1) and furnishing it into:

$$\Pi\Big(A(t),\dot{A}(t),t\Big)=U+T_s+T_{st}+T_b-\mathscr{W}, \tag{19}$$

where $U = U_b + U_m$ represents the total strain energy of the metastructure assuming no energy is stored through the shear deformation, and T_{st} and T_b represent the kinetic energies as follows. The kinetic energy of the striker is given as $T_{st} = \frac{1}{2}\overline{G}t^{*2}\dot{\Delta}_t^2$, where $\Delta_t = \sum_{i=1}^{n}\Delta_j$ denotes the total transverse displacement of the lattice. The total kinetic energy of the metastructure accounts for those of the interconnecting horizontal CDBs and vertical struts T_s and that of the curved beams T_b. The buckling of the curved beam in the lower layer induces two types of deformations: (*i*) the axial deformation of the vertical bars, and (*ii*) the rotation of the horizontal stiffeners at the joints between them, the curved beam, and the vertical bars. The vertical struts and horizontal stiffeners are assumed as rigid, inextensible elements, which travel at the same velocity as the curved beam in the lower layer. Hence, in the first phase of motion, the formulation of the kinetic energies considering the buckling of the CDB of the top layer accounts for the kinetic energies of the beam and striker only. Nevertheless, in the subsequent phases of motion, the mass of such rigid elements contributes to the kinetic energy formulations for the CDBs underneath.

The kinetic energy of the i^{th} curved beam is expressed as

$$T_{b,i}=\frac{h^2}{2}\int_{A_s}\dot{\overline{w}}_i^{\,2}\mu_s dA_s, \tag{20}$$

where $\mu_s = b\rho_b$ represents the mass per unit area of the beam. Since $dA_s = \widehat{\tau}ds_0$, ds_0 is determined by replacing w with W_0 in the expression of ds. Upon substituting Eq. (1) into Eq. (6) with the subsequent substitution of Eq. (2) into Eq. (20), we obtain

$$T_{b,i}=m_b h^2\sum_{j=1,5,9,}S_j\dot{A}_{i,j}^2, \tag{21a}$$

$$S_j=\begin{cases}(5s_0+l_0)/8s_0, & j=1\\ 5/4-l_0/2s_0, & j=3\\ 3/4. & j=5,7,9,\cdots\end{cases} \tag{21b}$$

where $m_b = \rho_b s_0 b\widehat{\tau}$ and ρ_b are the mass and density of the CDBs, respectively. The parameter S_j for other modes can be determined by substituting Eqs. (1)-(3) into Eq. (20) and evaluating the integral. The work done by the striker due to the conservative force P is expressed as $\mathscr{W}_{\mathrm{i}} = Ph\Delta_{\mathrm{i}}$. Using Eq. (17a-h), the dimensionless form of the total work done, kinetic, and strain energies are, respectively, expressed as:

$$\overline{\mathscr{W}}=\overline{P}\Delta_t, \tag{22}$$

$$\overline{T}_{b,i}=\overline{m}_i t^{*2}\sum_{j=1,5,9}S_j\dot{A}_{i,j}^2, \tag{23}$$

$$\overline{T}_{st,i}=2\overline{G}t^{*2}\sum_{j=1,5,9}\dot{A}_{i,j}^2, \tag{24}$$

$$\overline{U}_{b,i}=\frac{\omega_1^4}{4}\left(A_{1,i}-\frac{1}{2}\right)^2+\sum_{j=2}^{\infty}\frac{\omega_j^4 A_{j,i}^2}{4}, \tag{25}$$

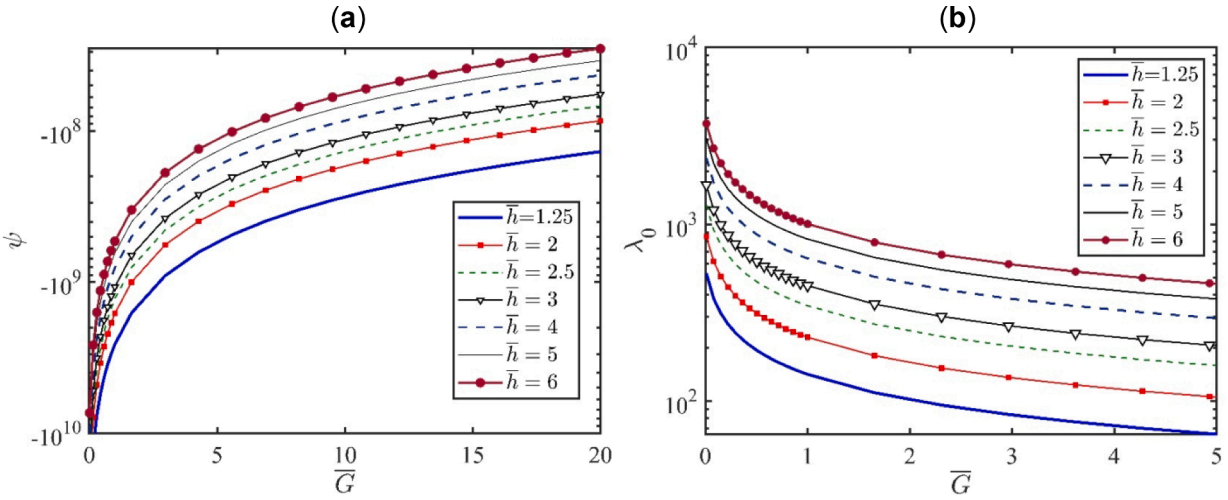

Fig. 3. Influence of bistability ratio on (**a**) the membrane stiffness, and (**b**) the modal frequency of vibration.

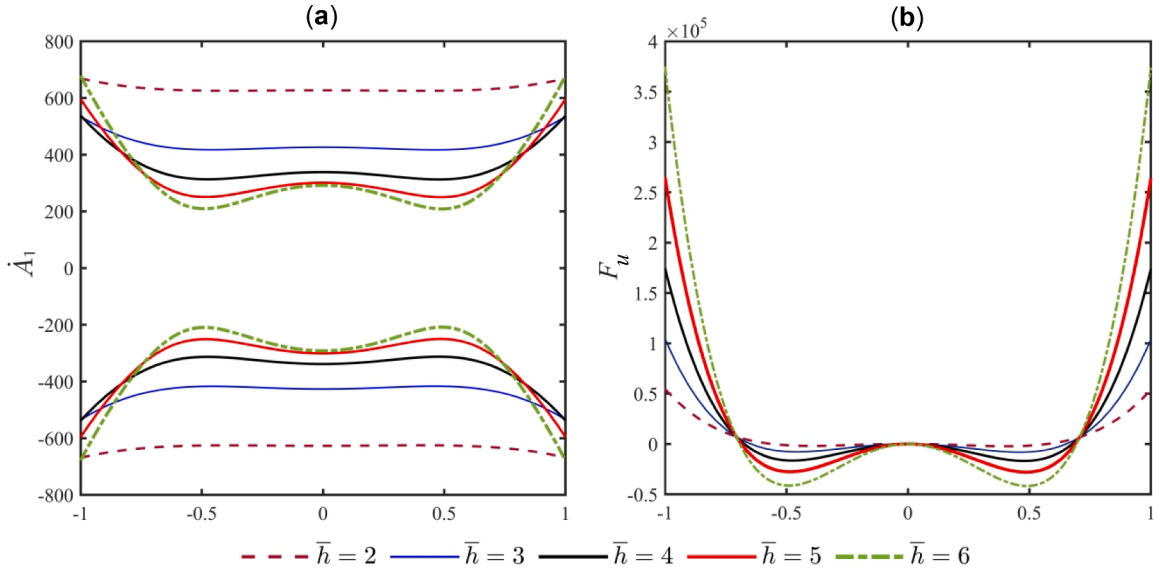

Fig. 4. (**a**) Phase-plane plot of the model given different bistability ratios. (**b**) Variation of the kinetic energy parameter $F_u = 2p_sA(t) - [1/2\psi A^4(t) + \lambda_0^2 A^2(t)]$ with $\overline{h}$.

$$\overline{U}_{m,i} = \frac{12l_0^2}{\widehat{\tau}^2}\left(\overline{s}_i - \frac{8\overline{s}_i^2}{\omega_1^2 + 16\overline{l}^2}\right). \tag{26}$$

In Eq. (24), $\overline{T}_{st,i}$ represents the portion of the kinetic energy of the striker that induces the motion of the corresponding beam. Substituting Eqs. (22)-(26) into Eq. (19) yields:

$$\overline{\Pi}_i = \sum_{j=1,5,9,} \left(2\overline{G} + \overline{m}_i S_j\right) t^{*2} \dot{A}_{j,i}{}^2 + \sum_{j=1,2,3,..} \frac{1}{4}\left(\omega_j^4 - \overline{p}\omega_j^2\right) A_{j,i}{}^2 + 2\overline{P} \sum_{j=1,5,9,...} A_{j,i} - \frac{\omega_1^4}{4} A_{1,i} - 4\overline{P}, \tag{27}$$

where the over-bar indicates the non-dimensional form of the quantity, while subscripts j and i refer to the mode and CDBs number, respectively. We may also drop the second index as the terms of displacement and velocities are identical for the CDBs in each layer. Using Hamilton's principle, the requirement that the trajectory $A(t)$ is a stationary point of the action functional $\mathscr{L} = \int_{t_1}^{t_2} \overline{\Pi}_i dt$ is satisfied provided that $\delta\mathscr{L} = 0$, the necessary and sufficient condition for which is the Euler-Lagrange expression as:

$$\frac{\partial \overline{\Pi}_i}{\partial A_{j,i}} - \frac{d}{dt}\frac{\partial \overline{\Pi}_i}{\partial \dot{A}_{j,i}} = 0, \tag{28}$$

such that

$$\partial(\overline{\Pi}_1) = \left(\frac{\left(\omega_1^4 - \overline{p}\omega_1^2\right)}{2} A_1 + 2\overline{P} - \frac{\omega_1^4}{4}\right)\partial A_1 + \sum\nolimits_{j=5,9,13,\cdots}^{\infty} \left(\frac{\omega_j^4 - \overline{p}\omega_j^2}{2} A_j + 2\overline{P}\right)\partial A_j. \tag{29}$$

By applying Eq. (28), a number of nonhomogeneous ordinary

differential equations (ODEs) are recovered with respect to every mode of deformation. From the results of numerical studies in the sequel, with the notion that mode 2 is constrained as assumed in (Mehreganian et al., 2021) it transpires that the predominant mode of beam deflection in the CDB is the first mode (Qiu et al., 2004), thus the influence of higher modes may be neglected in the study. Notably, in the static analysis, modes 2 and 3 yield linear force–displacement curves independent of the bistability ratio. Similarly, the consideration of higher modes ($j=5,9,13,\cdots$) gave rise to a marginal difference in the theoretical results of (Qiu et al., 2004). Regarding the top beam buckling, the form of the first ODE (Eq. (28)) is furnished as:

$$\lambda_0^2 A_1(t) + A_1^{\cdot\cdot}(t) + \epsilon_0 \psi A_1(t)^3 = \lambda_0^2 p_s, \tag{30}$$

where $\overline{Q} = \overline{h}^2/\overline{s}_1$, and

$$\psi = -\frac{24\overline{Q}\pi^4}{c_2 \epsilon_0}, \tag{31}$$

$$p_s = \frac{2-\overline{P}/\pi^4}{3\overline{Q}-4}, \tag{32}$$

$$\lambda_0 = \pi^2 \sqrt{\frac{6\overline{Q}-8}{c_2}}, \tag{33}$$

$$c_2 = 2(2\overline{G} + S_1\overline{m})t^{*2}. \tag{34}$$

The parameter ψ may be visualised as the (membrane) stiffness of the system. When $\psi = 0$, the theoretical solution boils down to a linearised ODE with a harmonic vibrational frequency of λ_0. The case of $\psi > 0$ corresponds to nonlinear hardening whereas for $\psi < 0$, the system is softening because with the increase in displacement, the system becomes softer (Feldgun et al., 2016). The former circumstance commonly occurs in the initially flat isotropic beams and plates subjected to transverse loading. The parameter ϵ_0 is a small perturbation number which may be chosen arbitrarily, herein selected as $\epsilon_0 = (h/l_0)^3$. The influence of bistability ratio $\overline{h}$ on the modal frequency λ_0 and membrane stiffness ψ is compared in Fig. 3.

It turns out that the ODE in Eq. (30) represents the inhomogeneous form of Duffing equation, representing the nonlinear forced oscillation of a spring. Using the separation of variables, the form of ODE boils down to $\dot{A}^2(t) = 2p_s\lambda_0^2 A(t) - [1/2\psi\epsilon_0 A^4(t) + \lambda_0^2 A^2(t)] + c$ with the integration constant being $c = \lambda_0^2\left(\frac{1}{32\lambda_0^2}\psi\epsilon_0 + a_1^2 + \frac{1}{4} - p_s\right)$, determined from the kinematic conditions at the onset of impact. With $\psi < 0$, the phase plane forms a saddle at the midpoint (Fig. 4).

A numerical scheme e.g. an iterative method may be pursued for the solution of Eq. (30) by initially disregarding the nonlinear term $\epsilon_0\psi A_1^3(t)$, resulting in a general linearised solution with the displacement field denoted as $A_1^{(0)}(t)$. The next iteration is sought by the substitution of $A_1^{(0)}(t)$ in lieu of the nonlinear component of Eq. (30). However, such a solution entails secular terms (such as $t\sin(t)$), whose presence brings about in non-harmonic diverging vibrations, whereby an unbounded growth of the amplitude emerges over time. Thus, the closed-form solution, representative of the physical harmonic vibration of the beam, is sought via the Poincaré-Lindstedt method (Mehreganian et al., 2019). To this end, the displacement field $A_1(t)$ may be perturbed using

$$A_1(t) = \epsilon_0^0 A_1^{(0)}(t) + \epsilon_0^1 A_1^{(1)}(t) + \epsilon_0^2 A_1^{(2)}(t) + O(\epsilon_0^3), \tag{35}$$

where the superscript denotes the order of the perturbed term of the displacement field. Similarly, the time and frequency of vibration would be truncated as

$$\lambda = \epsilon_0^0\lambda_0 + \epsilon_0\lambda_1 + \epsilon_0^2\lambda_2 + O(\epsilon_0^3), \tag{36}$$

$$\tau = \lambda t. \tag{37}$$

The terms λ_i $(i \geq 1)$ denote vibration pseudo-frequencies as they harmonise the displacement field vibration by increasing the frequency of the perturbed terms thus reducing their amplitudes, the exact values of which are determined explicitly from the solution of the displacement field. Substituting Eqs. (36) and (37) into Eq. (35), and ignoring higher-order terms, yields a polynomial in terms of ϵ_1. To this end, the coefficients of the $\epsilon_0^{(i)}$ should vanish to satisfy the differential equation, which results unequivocally in three sets of ODEs expressed as:

$$A_1^{(0)}(\tau) + A_1^{\cdot\cdot(0)}(\tau) = p_s, \tag{38}$$

$$\epsilon_1\left(\lambda_0^2\left(A_1^{(1)}(\tau) + A_1^{\cdot\cdot(1)}(\tau)\right) + 2\lambda_0\lambda_1 A_1^{\cdot\cdot(0)}(\tau) + \psi\left(A_1^{(0)}(\tau)\right)^3\right) = 0, \tag{39}$$

$$\epsilon_1^2\left(3\psi A_1^{(1)}(\tau)\left(A_1^{(0)}(\tau)\right)^2 + 2\lambda_0\lambda_2 A_1^{\cdot\cdot(0)}(\tau) + 2\lambda_0\lambda_1 A_1^{\cdot\cdot(1)}(\tau) + \lambda_1^2 A_1^{\cdot\cdot(0)}(\tau) + \lambda_0^2\left(A_1^{\cdot\cdot(2)}(\tau) + A_1^{(2)}(\tau)\right)\right) = 0. \tag{40}$$

The initial conditions at the onset of impact for the solution of Eq. (38) are $A_1^{(0)}(0) = 0.5$ and $\dot{A}_1^{(0)}$ equal to the magnitude of the initial modal velocity. The initial modal velocity field is obtained by satisfying the conservation of linear momentum by equating the momentum of the striker having a velocity $V_0 = h\overline{V}_0$ immediately before the impact with the combined total momentum of the striker and the metastructure immediately after the impact, i.e. $\dot{A}_1^{(0)}(0) = -\overline{GV}_0/[(2\overline{G} - \overline{m})\lambda_0]$. The solution of Eq. (38) then gives the dimensionless displacement as:

$$A_1^{(0)}(\tau) = p_s(1 - cos(\tau)) - \frac{sin(\tau)\overline{GV}_0}{(2\overline{G} - \overline{m})\lambda_0} + \frac{\cos(\tau)}{2}. \tag{41}$$

Substituting Eq. (41) into Eq. (39), while making use of Eqs. (31)-(33), we determine the next term of the displacement field as:

$$\begin{aligned} A_1^{(1)}(\tau) = \frac{3}{8\lambda_0^2}\Bigg(\left(a_1^2 + 5p_s^2 - p_s + \frac{1}{4}\right)\psi - \frac{8\lambda_0\lambda_1}{3}\Bigg)\Bigg(\Bigg(p_s - \frac{1}{2}\Bigg)sin(\tau) + a_1 cos(\tau)\Bigg)\tau + C_1\cos(\tau) + C_2\sin(\tau) + \frac{1}{64\lambda_0^2}\Bigg(8\Big(3a_1^2 \\ - p_s^2 + p_s - 1/4\Big)\left(p_s - \frac{1}{2}\right)\psi cos(\tau)^3 - 8\Bigg(a_1\Bigg(a_1^2 - 3p_s^2 + 3p_s - \frac{3}{4}\Bigg)sin(\tau) + 8a_1^2 p_s - 8p_s^3 + 8p_s^2 \\ - 2p_s\Bigg)\psi cos(\tau)^2 - 24\left(p_s - \frac{1}{2}\right)\Bigg(\frac{16}{3}a_1 p_s \psi sin(\tau) + \Bigg(a_1^2 - 5p_s^2 + p_s - \frac{1}{4}\Bigg)\psi + \frac{8\lambda_0\lambda_1}{3}\Bigg)cos(\tau) - 16\psi\Big(a_1^3 sin(\tau) + 4a_1^2 p_s + 12p_s^3 - 8p_s^2 \\ + 2p_s\Big)\Bigg)\Bigg), \end{aligned} \tag{42}$$

where $a_1 = -\overline{GV}_0/[(2\overline{G} - \overline{m})\lambda_0]$, while the integration constants are determined, by applying the initial kinematic conditions as:

$$\begin{cases} C_1 = \dfrac{\left(152a_1^2 p_s + 136p_s^3 - 12a_1^2 - 76p_s^2 + 22p_s - 1\right)\psi}{64\lambda_0^2}, \\ C_2 = -\dfrac{a_1\left(4\psi p_s^2 + 4\psi p_s - 16\lambda_0\lambda_1 + 3\psi\right)}{16\lambda_0^2}. \end{cases} \tag{43}$$

Obviously if $a_1 \neq 0$, or $p_s \neq \frac{1}{2}$, the term $\left(\left(p_s - \frac{1}{2}\right)sin(\tau) + a_1 cos(\tau)\right)\tau$ corresponds to a secular term. The condition to render the vibration harmonic is thus recovered by equating its coefficient to zero, giving:

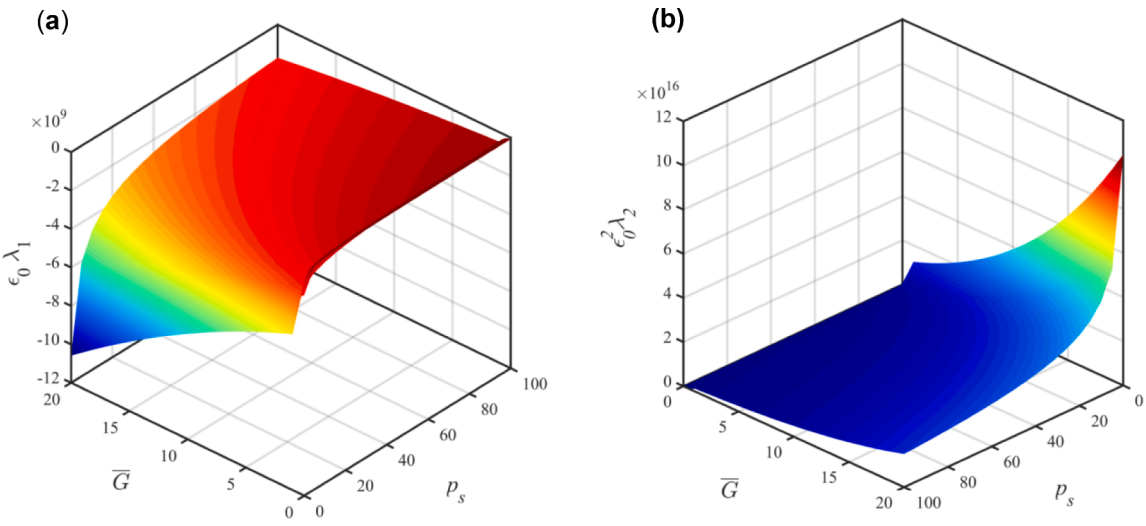

Fig. 5. Surface interaction of the load and striker mass with the pseudo frequencies of the CDBs: (**a**) the first, and (**b**) the second vibration pseudo-frequencies.

$$\lambda_1 = \frac{3\psi\left(5p_s^2 - p_s + a_1^2 + \frac{1}{4}\right)}{8\lambda_0}. \tag{44}$$

Referring to Eq. (40), the second perturbed term is sought by substituting Eqs. (42) and (41) into Eq. (40) and applying the same procedure. The solution to the further term of the displacement field boils down to:

$$\begin{aligned} A_2^{(2)}(\tau) = & f(\tau) + C_4\cos(\tau) + C_5\sin(\tau) + \frac{1}{98304\lambda_0^4}\Bigg(a_2 cos(3\tau) + a_3 cos(2\tau) \\ & + b_2 sin(3\tau) + a_4 cos(5\tau) + a_5 cos(4\tau) + b_3 sin(5\tau) + b_4 sin(2\tau) \\ & + b_5 sin(4\tau) + a_6 cos(\tau) + b_6 sin(\tau) + 156672\left(\frac{181}{17}p_s^4 - 10p_s^3\right. \\ & + \left.\left(\frac{110}{17}a_1^2 + \frac{143}{34}\right)p_s^2 + \left(-\frac{46a_1^2}{17} - \frac{29}{34}\right)p_s + a_1^4 + \frac{23a_1^2}{34} + \frac{21}{272}\right)\psi^2 p_s\Bigg), \end{aligned} \tag{45}$$

where the parameters $a_1 - a_6$ and $b_1 - b_6$ are expressed in Appendix A as Eqs. (A. 52)-(A. 61). The integration constants C_4 and C_5 are evaluated, in a similar fashion to the above, by dictating the kinematic conditions of the displacement and velocity fields at the onset of impact, as:

$$\begin{aligned} C_4 = & \frac{1}{6144\lambda_0^4}\Bigg(\left(-51912p_s^5 + 42444p_s^4 + \left(-20448a_1^2 - 16158\right)p_s^3\right. \\ & + \left(10248a_1^2 + 2973\right)p_s^2 - \left(9432a_1^4 + 6354a_1^2 + 366\right)p_s + 300a_1^4 - 69a_1^2 \\ & - 3\Big)\psi^2 + 12752\left(\frac{95p_s^3}{797} - \frac{541p_s^2}{1594} - \left(a_1^2 - \frac{221}{3188}\right)p_s - \frac{99a_1^2}{1594}\right. \\ & + \left.\frac{33}{6376}\right)\lambda_1\lambda_0\psi + 3072\left(p_s - \frac{1}{2}\right)\lambda_0^2\left(\lambda_0\lambda_2 + \frac{\lambda_1^2}{2}\right)\Bigg), \end{aligned} \tag{46}$$

$$\begin{aligned} C_5 = & -\frac{a_1}{128\lambda_0^4}\Bigg(\Bigg(-1157p_s^4 + 676p_s^3 - \left(1926a_1^2 + 412\right)p_s^2 \\ & + \left(232a_1^2 + \frac{143}{2}\right)p_s + 15a_1^4 - 6a_1^2 - \frac{15}{16}\Bigg)\psi^2 \\ & - \frac{4\lambda_0\left(9a_1^2 + 1189p_s^2 - 581p_s - \frac{27}{4}\right)\lambda_1\psi}{3} - 128\lambda_0^3\lambda_2 - 64\lambda_0^2\lambda_1^2\Bigg). \end{aligned} \tag{47}$$

The function entailing the secular term $f(\tau)$ is expressed as:

$$f(\tau) = \left(X_1 - \frac{(128p_s - 64)\lambda_2}{128\lambda_0}\right)\tau sin(\tau) + \left(Y_1 - \frac{a_1\lambda_2}{\lambda_0}\right)cos(\tau)\tau, \tag{48}$$

where

$$\begin{aligned} X_1 = & -\frac{81}{128\lambda_0^4}\Bigg[\psi^2\left(a_1^4 p_s + \frac{5}{54a_1^4} + \frac{350}{27}a_1^2 p_s^3 - \frac{131}{27}p_s^2 a_1^2 + \frac{5}{9p_s a_1^2} - \frac{1}{54}a_1^2\right. \\ & + \left.\frac{515}{27}p_s^5 - \frac{115}{6}p_s^4 + \frac{224}{27p_s^3} - \frac{91}{54}p_s^2 + \frac{53}{432p_s} - \frac{1}{864}\right) + \frac{\lambda_0^2(128p_s - 64)\lambda_1^2}{162} \\ & - \frac{244\psi\lambda_0\lambda_1\left(p_s a_1^2 + \frac{3}{122}a_1^2 + \frac{65}{61}p_s^3 - \frac{67}{122}p_s^2 + \frac{35}{244}p_s - \frac{1}{488}\right)}{81}\Bigg], \end{aligned} \tag{49}$$

$$\begin{aligned} Y_1 = & 1\Big/\Big(98304\lambda_0^4\Big)\Big(\Big(-495360a_1 p_s^4 + 322560a_1 p_s^3 \\ & + \left(-299520a_1^3 - 119808a_1\right)p_s^2 + \left(-18432a_1^3 + 5760a_1\right)p_s \\ & + 11520a_1^5 - 4608a_1^3 - 720a_1\Big)\psi^2 - 9216\lambda_0\lambda_1\left(\frac{55}{3}a_1 p_s^2 - \frac{23}{3a_1 p_s} + a_1^3\right. \\ & - \left.\frac{3}{4a_1}\right)\psi - 49152\lambda_0^2 a_1\lambda_1^2. \end{aligned} \tag{50}$$

Through algebraic manipulation, with $X_2 = X_1 - (128p_s - 64)\ \lambda_2/128\lambda_0 = R_0\cos(\phi)$ and $Y_2 = Y_1 - \frac{a_1\lambda_2}{\lambda_0} = R_0\sin(\phi)$, while $\phi = \tan^{-1}Y_2/X_2$, the expression for the second vibration pseudo-frequency can be determined as (51). The interactions of the striker mass and load coefficient with the pseudo-frequencies are plotted in Fig. 5.

$$\lambda_2 = \frac{4\left(X_1 p_s - \frac{1}{2}X_1 + a_1 Y_1\right)\lambda_0}{4a_1^2 + 4p_s^2 - 4p_s + 1}. \tag{51}$$

3.2. Subsequent phases of motion $\left(t_{d,i} \le t \le t_{d,i+1}\right)$

Following the full compression of the upper CDB at the top layer, at transition time $t_{d,1}$ the lower CDB of the top layer initiates buckling while the stiffness of the upper CDB is completely lost and its corresponding energy components are eliminated from the Euler-Lagrange energy function $\mathscr{L}$. It transpires that the form of the ODE (Eq. (30)) and the ensuing Poincaré-Lindstedt ODEs remain valid but entail the displacement field $A_{1,2}$ in lieu of A_1. It is assumed that the striker

Table 1
Characteristic dimensions of the NSHM models.

Parameter	Magnitude (mm)	Parameter	Magnitude (mm)
H_d	16.5	l_0	57
H_a	24	l_b	16.5
H_w	3	τ_s	2.5
h	4,6,7,8,10,12	τ_{cb}	1.75
h_{cb}	3	τ_b, τ_d	2
h_b	12	τ_w	3

remains in contact with the lattice surface during the subsequent phases of motion, while its velocity $\overline{V}_0$ now accounts for the total velocity of the lattice CDBs underneath, or $\dot{\overline{\Delta}}(\tau) = -2\lambda\dot{A}_1(\tau)$. The kinematic conditions of the displacement and velocity fields between the two CDBs must be satisfied at the transition time $t_{d,1}$. In a similar manner, following the full snap-back of the inverted beam in the top layer at $t_{d,2}$, the CDB in the bottom layer undergoes buckling while its initial kinematic conditions are derived from those of the previously buckled CDB. The expression of the displacement field for the successive CDBs is derived by the substitution of $\tau_{i+1} = \lambda(t - t_{d,i})$ in place of τ into Eqs. (41), (42), and (45). The total displacement of the lattice is defined as the cumulative displacements of the CDB pairs in the post-buckled state.

4. Numerical analysis and discussion

The accuracy of the analytical model for the response of an individual CDB pair underlies the response of the entire lattice. Several three-dimensional finite element (FE) models were thus set up in ABAQUS® Explicit to validate the analytical model, in two folds. In the first, we examined the response of the individual CDB considering the impact of a striker with velocities $V_0 = 0.5$, 0.75, 1, 2, and 4 m/s, $G = 1$ and 2 kg, and a CDB apex height of 8 mm. In the second, the influence of the bistability ratio $\overline{h} = h/t$ on the impact resistance of the models was examined both numerically and analytically.

The striker in both models was designed as a rigid capsule, having a 10 mm radius of projection and a cylindrical height of 35 mm, which was discretised with 36 R3D3 discrete rigid elements. The striker comprises a hemispherical nose and a cylindrical extension of the body. The striker's lateral motion and rotations were constrained and it was permitted to move in the vertical direction only. The particular choice of this shape is due to the fact that a point impact is more likely to occur than a distributed one, besides any nose shape could be plausible, but a simple one indicates a more suitable point of departure. In practical applications, the impact is seldom uniformly spread over the entire lattice surface and is normally restricted to a localised area.

Both the single beam and the lattice were made of polyamide 11 with Young's modulus of 1582 MPa, a Poisson's ratio of 0.33, and a mass density of 1.04 g.cm^{-3}. This material is favourable as it is classified as a lightweight, isotropic, ductile, and highly flexible material. The models here were assumed to be perfectly elastic with the prescribed geometric nonlinearities. The FE models were discretised with a minimum element size of 0.7 mm of S4R shell elements and a thickness of 15 mm. This gave a total of 34,564 S4R elements for the lattice, and the element length-to-beam thickness ratio as one-third. The S4R elements are general, doubly curved shell elements with reduced integration and hourglass control for which 17 Simpson integration points through the thickness were prescribed. These elements' deformation was controlled with finite membrane strains. The relevant geometric parameters of the CDB were the same in both models, as stated in Table 1. A penalty contact type with a coefficient of friction of 0.3 was assumed for each contact pair of the structural elements in both models. By default, the shell offset and thickness were accounted for by contact constraints in ABAQUS. The models using conventional S4R shell elements and continuum shell elements (SC8R, which are 8-node hexahedron shell elements with finite membrane strains (Corp, 2005) exhibit a faster rate of convergence than those modelled with C3D8R continuum elements (which are 8-node linear elements, referred to as the 'brick' elements) or M3D4R membrane elements (Mehreganian et al., 2021).

The lattice structure was designed with three constituent cells in the horizontal direction and two in the vertical direction, the configuration, and dimensions of which are set out in Fig. 6. The NSH lattice was subject to an impact loading by the (same) striker but with a 5-kg mass and the impact velocity of 2 m/s in a Dynamic/Explicit model, to yield a momentum equivalent to a high-velocity projectile with a 20-g mass and a 500-m/s speed thus provided the strain rate sensitivity effects are discarded, the choice of the impactor highlights two purposes, ((i) the validity of the analytical model due to impact by the 'local' (conforming) impactors, and (ii) a benchmark analysis for the impact response of the NSHM due to the striker impacts of various velocities. For the individual CDB, the beam pair was clamped at either side, while the lattice was fixed at the bottom. The sides of the lattice were prescribed symmetric boundary conditions.

According to the static analyses conducted by researchers (Restrepo et al., 2015; Correa et al., 2015; Mehreganian et al., 2021), the force–deformation landscape of the lattice is characterised by three regimes.

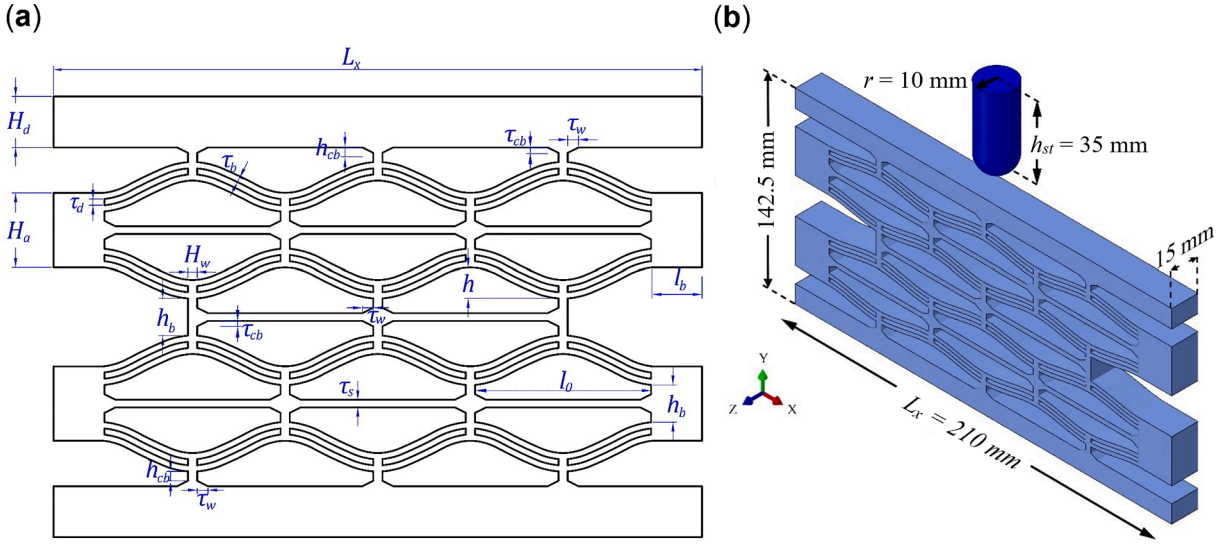

Fig. 6. (**a**) Geometric parameters of the NSHM lattice. (**b**) Schematics of the finite element model (with $\overline{h} = 3$).

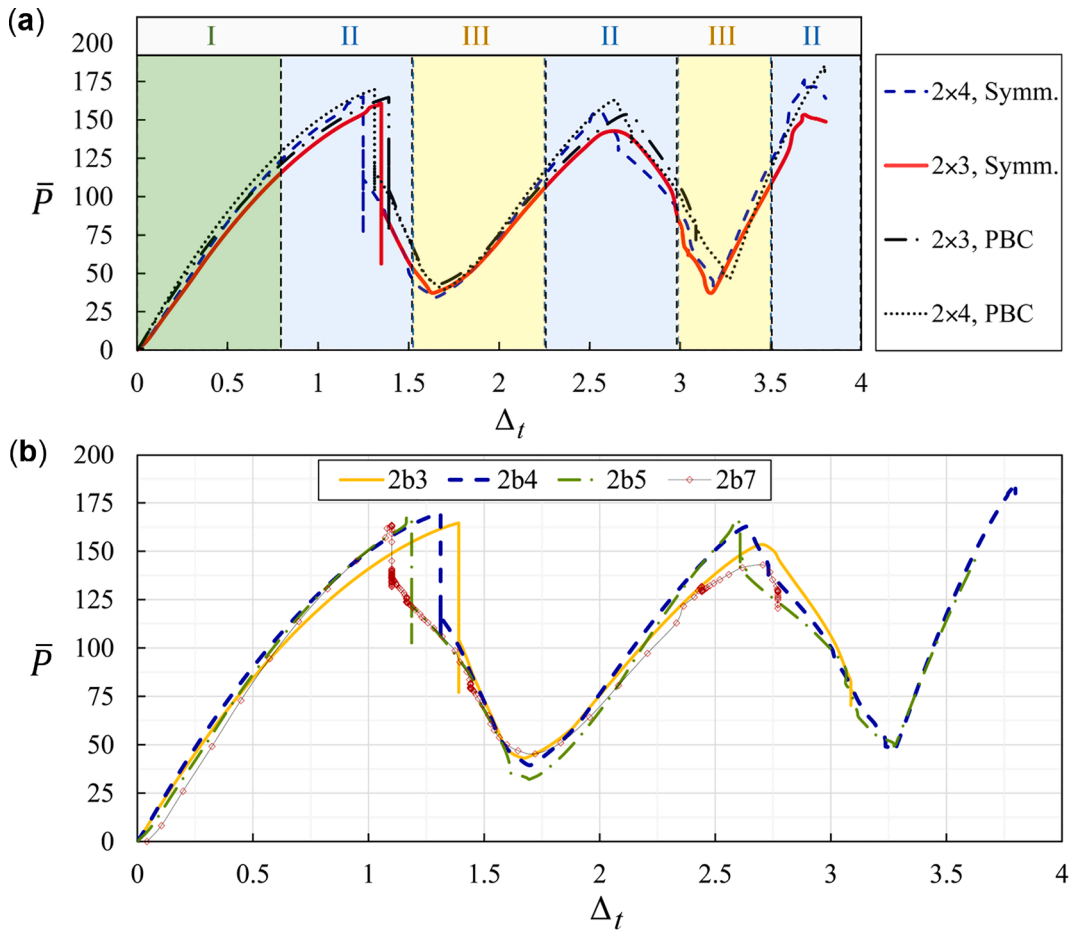

Fig. 7. (**a**) Force-displacement of the NSHM lattices with periodic boundary conditions (PBC) and symmetric (Symm.) boundary conditions. Regime I corresponds to the initial deformation of the lattice, regime II represents the initiation of the phase transformation from mode 1 to 3, while regime III is characterised by the snap through to the inverted beams. (**b**) Influence of the number of unit cells on the lattice with PBC response.

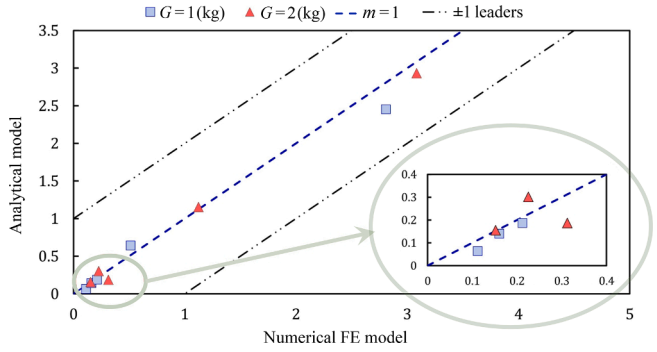

Fig. 8. Comparison of the analytical and numerical results of the normalised maximum deformation Δ_t for an individual CDB pair.

Regimes I and III are governed by positive stiffness as they are attributed to the deformations in stable configurations, with the potential energy at the point of local minima. Regime II corresponds to the negative slope which corresponds to the phase transition from mode one to three (see Fig. 7a). As the configuration of the CDB during this phase is unstable, it immediately transforms into the stable equilibrium phase (regime III) with the CDB profile reversing. This lattice was loaded transversely at the top surface with a loading rate of 0.01 mm/s, in line with the static analyses performed experimentally (Correa et al., 2015).

For microscale periodic lattices, the Representative Volume Element (RVE) can be prescribed with the periodic boundary conditions (PBC), which is specified by displacement differences of the pair of two opposite parallel boundary surfaces of a repeated unit cell (Al Kassem and Weichert, 2009; Tian et al., 2019; Bouaoune et al., 2016), and may be applied on the surface node of the model through a linear multi-point constraint. The displacement difference on a pair of parallel opposite k^{th} boundary surfaces can be written as $u_i^{k+} - u_i^{k-} = \varepsilon_{ij}^0\left(x_j^{k+} - x_j^{k-}\right) = \varepsilon_{ij}^0 \Delta x_j^k$, with the indices $k+$ and $k-$ identifying the k^{th} pair of two opposite parallel boundary surfaces of an RVE composite, when each point x_j^{k+} on a boundary $\partial\phi^+$ of the RVE is associated with a unique point x_j^{k-} on the opposing part $\partial\phi^-$ of the RVE (Tian et al., 2019).

It can be postulated from Fig. 7 that, despite the relatively coincidental curves of the NSHM lattices with the PBC to those without PBC, the latter aids minimisation of vibration jumps in the structure (at Δ_t 1.35), a phenomenon which occurs due to the residual vibrations of the beams in the lower layers in the first stage of deformation, while these beams' buckling is yet to emerge. At the same time, snap-through buckling of the beams in other layers initiates. In the force–displacement plots of the structure, this is characterised by a sudden fluctuation in the force without any changes in the deformation. For the simulations of the dynamic problem of the RVE composite using the Explicit FE solver, Garoz et al (Garoz et al., 2019) prescribed dummy nodes of prescribed mass and the associated PBC linear constraints were applied. These nodes were detached from the model and served as reference points.

In addition, similar to the results of (Al Kassem and Weichert, 2009), the difference between the PBC and the results with homogenous boundary conditions (HBC, our case in dynamic impact analysis) is

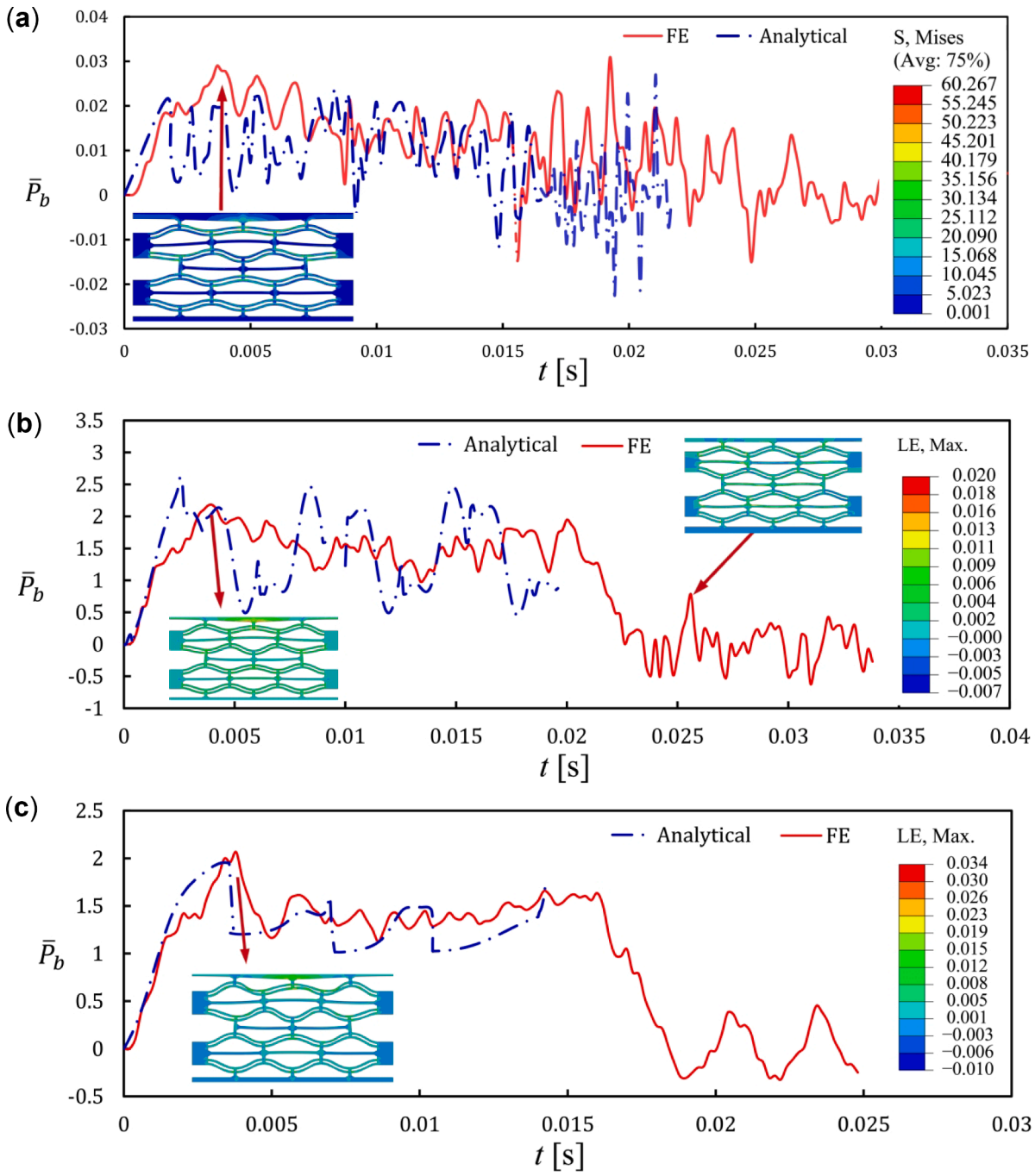

Fig. 9. Analytical versus numerical force–time histories of models with (**a**) $\bar{h} = 3$, (**b**) $\bar{h} = 4$, and (**c**) $\bar{h} = 5$.

minimal. As the cases have marginal differences, the homogeneous boundary conditions are still valid for the structures of meso- and higher length-scales such as the model under consideration here. It should also be noted that the models with HBCs are more computationally efficient and less time-consuming to run than those with the PBCs, particularly when dealing with dynamic problems which must be solved using the conditionally stable Explicit solver.

The influence of the number of unit cells included on the response of the NSHM lattice to the transverse load is depicted in Fig. 7, where the notation "*mbn*" denotes the structural arrangement with *m* constituent cells in the horizontal direction and *n* cells in the vertical direction. Except for the first peak, the magnitude of the load and the associated displacement for all lattice sizes virtually converge to the same curve. While the displacement associated with the first peak of different lattice sizes reduces with the increase in the number of constituent cells in the horizontal direction, the first peak magnitudes of the load remain relatively unaltered. It should further be noted that the displacement difference boundary conditions for the PBC may not always guarantee the traction continuity conditions (Al Kassem and Weichert, 2009). Despite the differences in the FE solver computations due to the influence of mesh size and element type, the force–displacement convergence is still satisfied.

Finally, in the case of mass impact problems, specifically, those associated with the striker impacts, the PBC will become irrelevant, as it ensures the stress continuity at parallel opposite boundaries, while due to the localisation of the impact and distinguishably different stress evolution at the contact interface compared to other types of laterally induced motion by loading the NSHM statically or via periodic dynamic

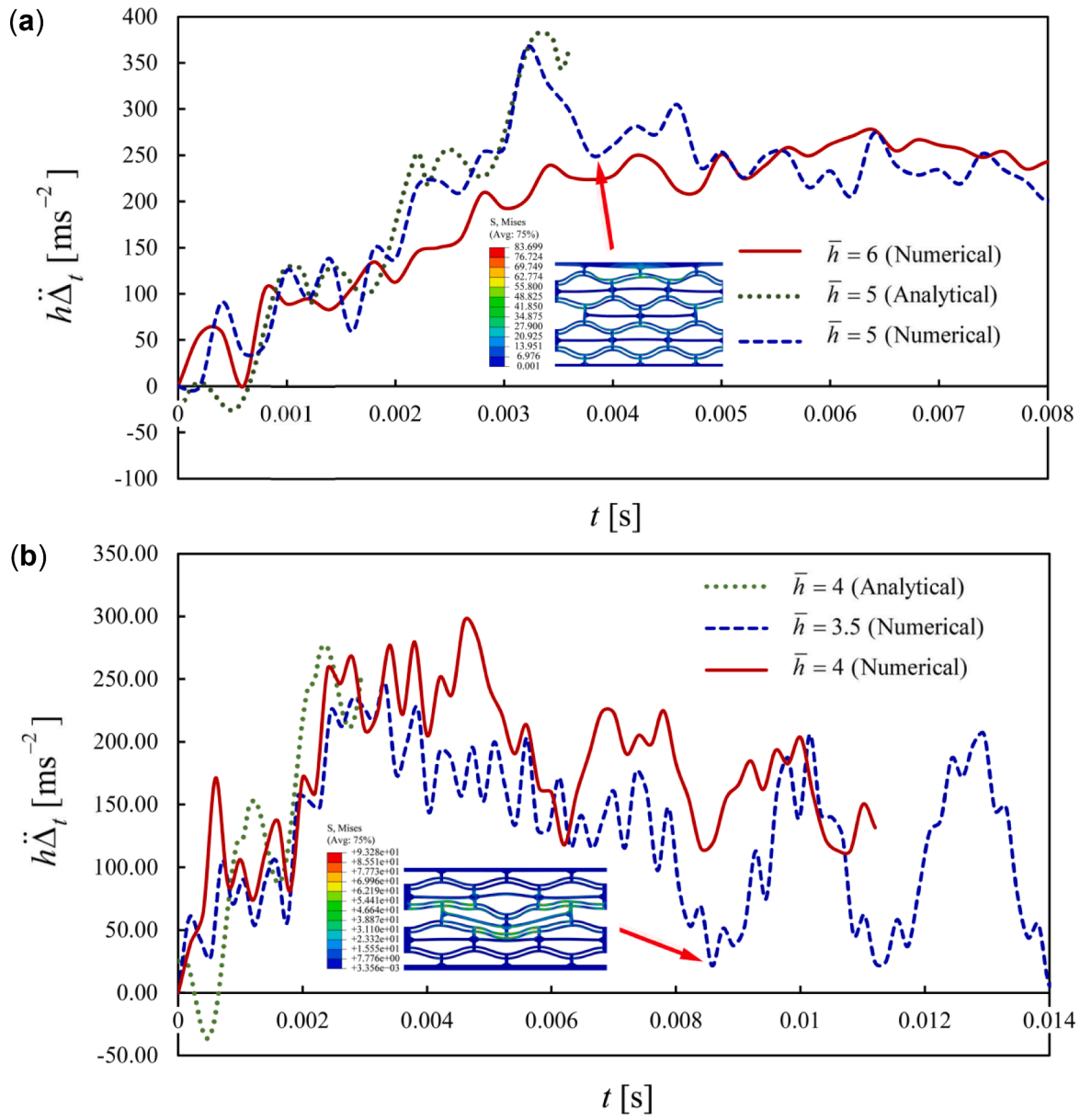

Fig. 10. Comparison of the lattice acceleration determine analytically with the numerical one for (**a**) $\overline{h} = 5$ and $\overline{h} = 6$, and (**b**) $\overline{h} = 3.5$ and $\overline{h} = 4$.

excitations continuity is violated more often than not.

As plotted in Fig. 8, the analytical model captures the maximum displacement field in the individual CDB pair with high precision. In the case where the greatest difference between the two models emerges, beyond the striker's initial momentum of the 2 N.s, the striker induces saddle-node bifurcation (snap-through) wherein the CDB undergoes a phase transformation from a stable state to an unstable one. In the lower bound of the abscissa in the figure ($\Delta_t < 0.5$), however, small dynamic perturbations occur, and the first peak in the displacement history occurs at the first phase of motion.

In Fig. 9a-c, we compare the analytical versus numerical predictions of the force–time histories of the lattices with $\overline{h} = 3, 4,$ and 5, respectively. The analytical plots account for three phases of motion while the striker is in contact with the lattice. Although the frequencies of the response curve from the two plots (Analytical vs FE) differ, apart from the first 3 ms of the model with $\overline{h} = 3$, the force–time histories are consistent. The captured peak force from the FE models also shows good agreement with that of the analytical one, with the percentage of error being 6.3%,7.9%, and 2.6% for $\overline{h} = 3, 4,$ and 5, respectively, which is bounded to 8% in all cases. It should, however, be recognised that the response in the lattice is more complex and the CDBs in each constituent cell undergo residual vibrations erratically, leading to the erratic shape of the ordinate in Fig. 9. However, the analytical model can capture the generic trend of the first peaks in the initial phase followed by the residual ones in subsequent phases. In the lattice with a CDB of a lower bistability ratio, it is interesting to observe more irregular force fluctuations.

A comparison of the acceleration of the CDBs with those of the analytical results is drawn in Fig. 10. Except for the initial estimation of the ordinate during the first cycle (the first 1 ms), the transient inertia from the analytical model corroborates favourably with the numerical counterparts. The analytical model predicts the critical points (peaks) of the inertia with good precision. Notably, as discernible from Fig. 11, due to the increase in stiffness, the magnitude of the permanent displacement (Δ_t) of the structure reduces as the initial curvature (bistability ratio) increases. The ordinate of Fig. 11 is determined from the derivative of the total elastic strain energy of the lattice with respect to Δ_t, which is then normalised and scaled by the number of the CDBs. The

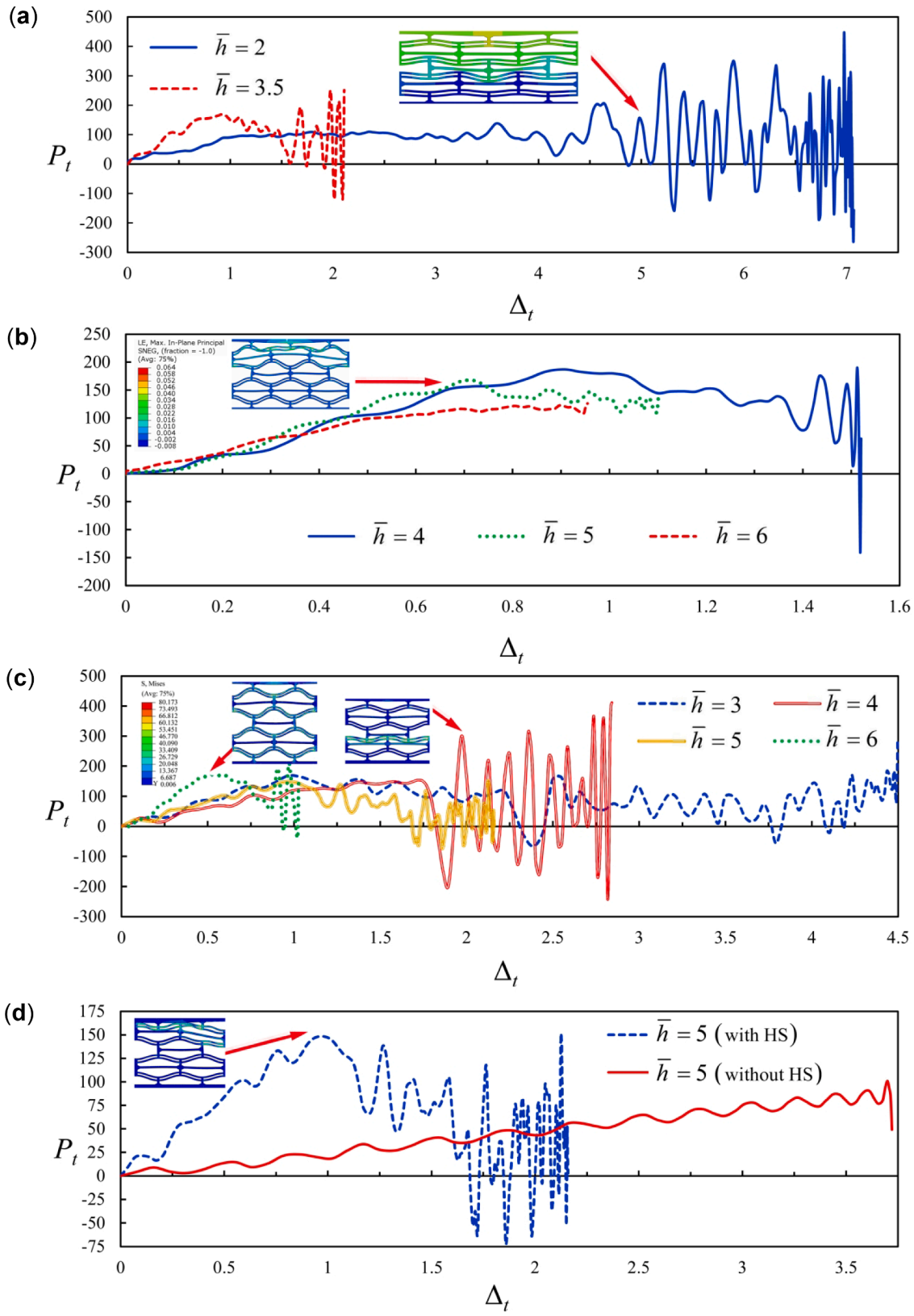

Fig. 11. Numerical FE results of the force–displacement plots for various bistability ratios, where the abscissa and ordinate represent the total displacement of the lattice and the strain energy derivative (applied force), respectively. (**a**) Force-displacement plots of models with $\bar{h} = 2$ and 3.5, with captured logarithmic strains at the peak load. (**b**) Force-displacement plots of models with $\bar{h} = 4 - 6$. (**c**) Force-displacement plots of the 2×2 cell models with $\bar{h} = 3 - 6$. (**d**) Force-displacement plots of models with $\bar{h} = 5$, with and without the horizontal stiffeners.

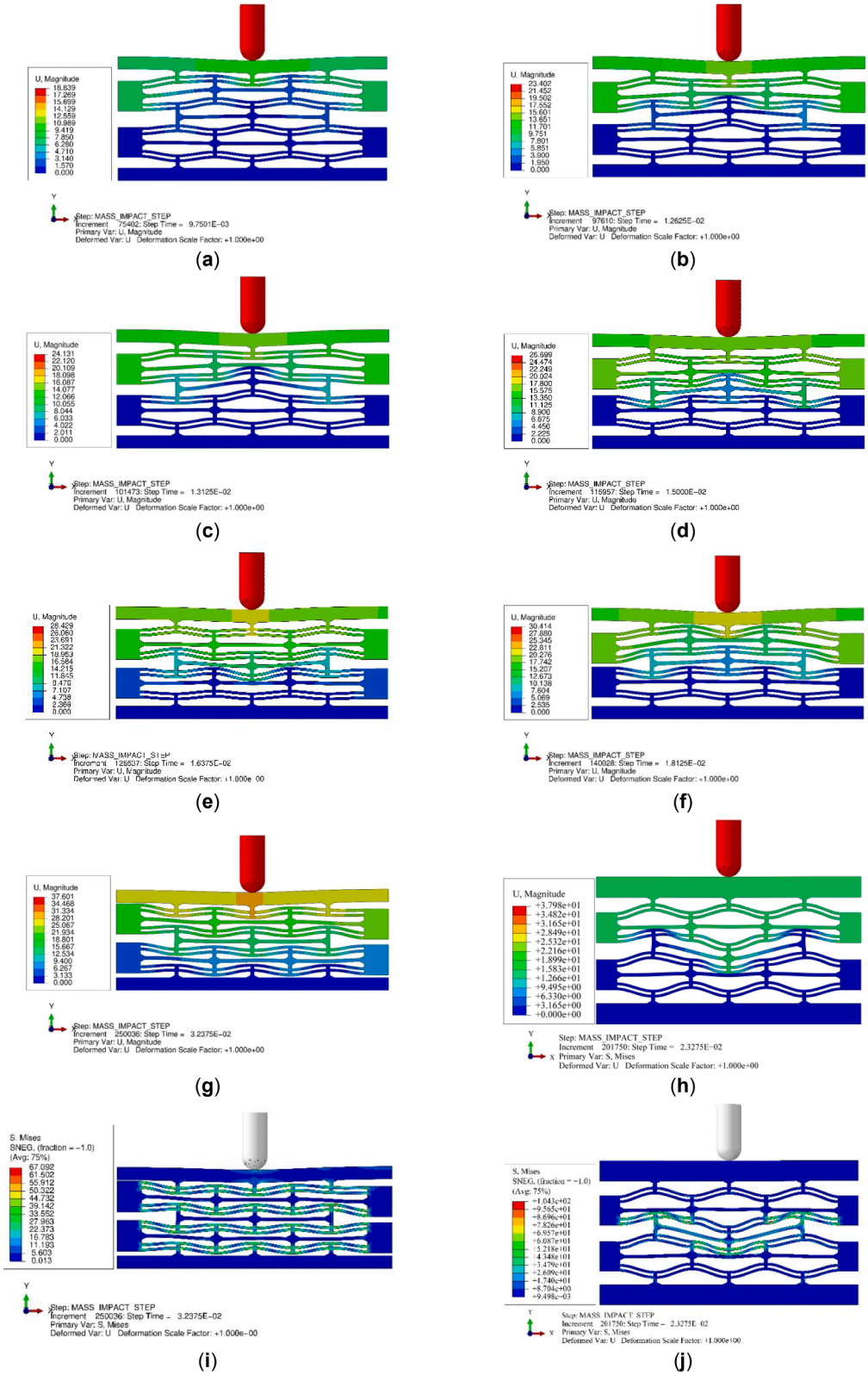

Fig. 12. Schematics of the lattice profile shape and Mises stresses in the lattice with $\overline{h} = 2$: (**a**) the initial curvature change and buckling; (**b**) the snap-back of the lower CDB in the first layer; (**c** & **d**) the snap-buckling of the inverted beams of the lower layer; (**e** & **f**) the full snapping deformation of the top beams in the lower and upper levels; (**g** & **i**) the full compression of the NSH lattice with deformations and Mises stresses of the model, respectively. (**h** & **j**) the deformation and Mises stress distribution in the lattice with $\overline{h} = 3.5$ at the point of middle beams snapping phenomena, respectively.

general trends in Fig. 11a-c is a smooth approach of the force to a local maximum the position of which shifts to the left at the expense of a high $\overline{h}$, followed by an oscillatory reduction. Interestingly, the local maxima of the force P_t reach a maximum limit up to 187 N with the increase of the bistability ratio, up to $\overline{h} = 4$; though P_t attenuates subsequently as $\overline{h}$ increases further. Such a trend may be elucidated with reference to the magnitude of the curved beam stiffness as presented in Fig. 2.

As illustrated in Fig. 11, significant fluctuations in the magnitude of the force are observed within a small variation of the displacement field in the vicinity of the maximum displacement limit for $\overline{h} = 2, 3.5,$ and 4 in Fig. 11a and $\overline{h} = 4 - 6$ in Fig. 11b; the oscillations in P_t diminish in the models with amplified $\overline{h}$. These variations may have arisen because of

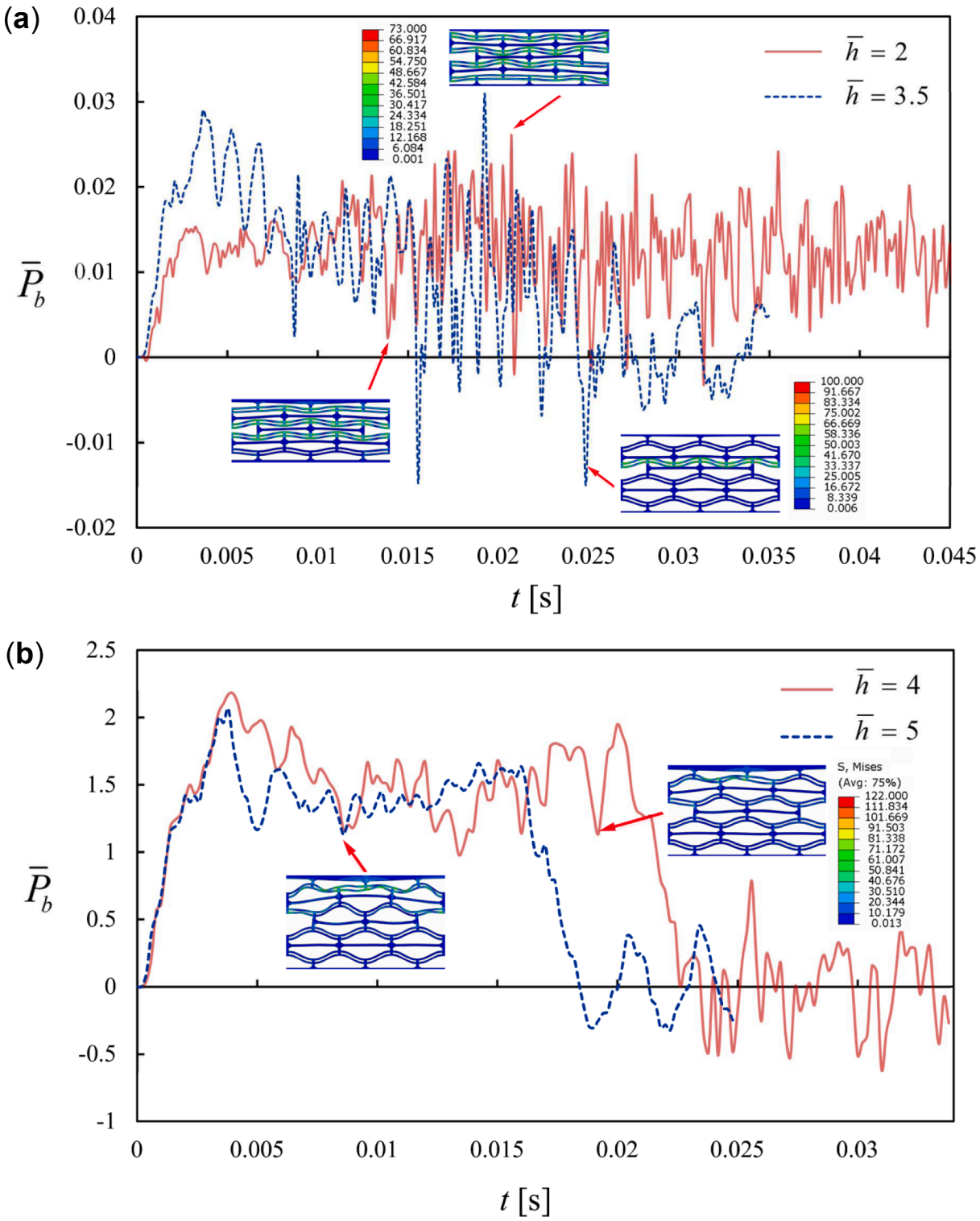

Fig. 13. Transient reaction force plots $\overline{P}_b$ in the boundaries of the lattice, where the contour legends represent the Mises stress magnitudes of the lattice. (**a**) Force-displacement plots of $\overline{h} = 2$ and 3.5 models. (**b**) Force-displacement plots of $\overline{h} = 4$ and 5 models (the two schematics at 0.005s and 0.02s of sub-figure 'a' share the same legend, and so do those of sub-figure 'b').

the small vibrations of the CDBs in the top layer at the associated time points without undergoing snap-through/snap-back. The magnitude of the strain energy, although escalating monotonically in all models, oscillates temporarily due to such vibrations. Furthermore, some non-homogeneous deformations of the CDBs arise during the lattice deformation inducing relative displacements within the CDBs, particularly in the models of higher $\overline{h}$. The buckling order of the beams varies accordingly and at the initial velocity of 2 m/s, only the uppermost beams of metastructures with $\overline{h} > 4$ experience buckling. Upon the impact of the striker, the presence of deformation modes other than modes 1 and 3 is discerned in the lattice employing 2×2 cells, analysed in Fig. 11c for the sake of comparison. This was primarily associated with the buckling

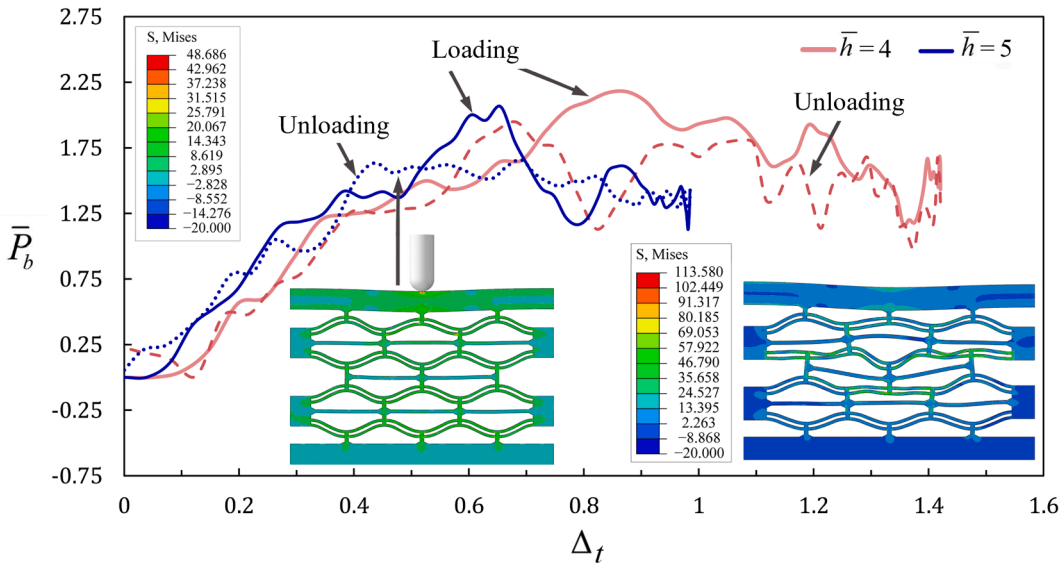

Fig. 14. The loading–unloading cycle of the lattice response upon striker impact for $\overline{h}=4$ and $\overline{h}=5$.

of the beams across the central (vertical) axis of symmetry, while the CDBs of the lowest level remained undeformed. Such a response would induce rotations in the horizontal and vertical struts on either side of the central axis. While the rotation of the vertical struts may be associated with mode 2 being not fully constrained, this rotation was only observed in one model. Evidently, the height of the centre clamp can affect the degree of constraints imposed on the CDBs in each layer, while the increase in the height of the centre clamp also indicates the overall increase in the lattice height. In the region close to the two stable positions, the motion of the CDBs is independent of the centre clamp height. Nevertheless, according to (Qiu et al., 2004), the force–displacement plots of the CDBs with mode 2 fully constrained, i.e. with the optimised gap between the beam pairs, the stiffness and geometry of the centre clamp, and the beam length/thickness ratios, are very close to the ones in which mode 2 is partially-constrained. Thus, while further studies are required to investigate the optimum lattice topology to eliminate the interference of other modes with the predominant mode of vibration, the analytical results developed in the previous section can provide a sound assessment of the lattice response. Lastly, with an increase in cell numbers in parallel to 3 and more, the CDBs at the bottom layer remained intact and thus the overall elastic vibrations of the CDBs in the bottom layers (unbuckled beams) due to the impact on the upper layers are bounded.

The bistability of the lattice also aids in higher energy entrapment of the structure. The boundary conditions and the number of cells do not influence the sub-wavelength energy entrapment trends with the bistability ratio, a common feature of multistable architected metamaterials/metastructures (Shan, 2015).

Fig. 11d draws comparisons of the lattices made of 2×2 cells with and without the horizontal beams. The response of the latter model is characterised by a monotonic increase of the load whilst that of the former undergoes a snap-back buckling response, in tandem with a pronounced reduction of the maximum transverse displacement at the expense of the higher loading magnitude. In contrast to the general pattern of the loads with the stiffeners, the loading distinctively increases monotonically in the model without them, while the path of the load curve reveals infinitesimal vibrations. The presence of stiffeners is therefore crucial for the desired phenomena of snap-back and snap-through which aid in energy entrapment in the metastructure.

The profile shapes and Mises stresses of the 2×3 lattice with $\overline{h}=2$ (the only model that underwent full compression) is illustrated in Fig. 12. Within the initial time limit of 10 ms, the uppermost CDBs undergo a curvature reverse while the remaining CDBs retain their original shape or will be on the verge of buckling. By time $t = 13.2$ ms, the loading would have reached its maximum limit, followed by the snapping back of the inverted double-curved beams of the top level. The transfer of the dilatational waves from the contact interface between the striker and the lattice forces snap-back buckling in the inverted beams of the lower level until full compression at $t = 23.2$ ms occurs. Clearly, due to the flexibility of the lattice, the contact point of the striker with the lattice exhibits some deformations giving an initial conical profile shape. The captured axial deformation of the curved beam relative to the transverse counterpart was considerably diminutive.

In Fig. 13, the non-dimensional reaction force $\overline{P}_b$ captured at the midpoint of the bottom support is compared for various bistability ratios. Such a parameter is likewise scaled according to the number of CDBs. The lower the bistability ratios ($\overline{h} < 4$), the higher the number of fluctuations of reaction forces over the time history of motion, The models with elevated $\overline{P}_b$ exhibit a higher oscillation frequency as well. The time point of the separation of the striker from the structure was monitored as 265 ms for $\overline{h}=3.5$ and 2 ms for $\overline{h}=4$. As such, higher bistability ratios yield higher lattice stiffness which in turn lowers the duration of the impact. Upon detachment of the striker from the lattice, the stored energy is released and results in the residual vibrations in the CDBs (Fig. 13b) hence the spectrum of the force oscillates about zero (the local minimum of the equilibrium point) before all the stresses within he system vanish. As observed, the duration of such oscillations is prolonged with the models of lower $\overline{h}$. According to Fig. 13b, at the time points of 5 ms and 18.6 ms, respectively, snap-back buckling occurs for the models $\overline{h}=5$ and $\overline{h}=4$, although the top beam of the lower level and the inverted beams of the top level of the latter design undergo snapping at $t = 13.4$ ms, corresponding to the minimum magnitude of the force. The highest displacement in the CDBs is associated with the middle-inverted beam of the top level. Interestingly, except for the model $\overline{h}=2$, no CDBs in the lowest level exhibited curvature change.

As the striker and the lattice remain in contact up to rest, the striker's kinetic energy is fully transferred to the strain energy of the lattice which manifests in its transverse deformations, until all the kinetic energy of the striker is transferred and its momentum vanishes. Thereafter, the unloading phase initiates (Fig. 14), when the lattice relieves the stored energy and recovers to its original shape, pushing the striker back (upwards) in the opposite direction. This is depicted by the reduction of the reaction force to zero but with fluctuations around this stable position (Fig. 13).

5. Concluding remarks

This work deals with the impact resistance of a metamaterial lattice structure referred to as the Negative Stiffness Honeycomb Metastructure (NSHM) model made of isotropic material. Utilising the Euler-Lagrange equations of motion and the Poincaré-Lindstedt perturbation technique, analytical solutions were derived and compared against parametric finite element numerical models. It was shown that the CDBs would generally experience bistability due to a transition from mode 1 to mode 3. The transient dynamics of the forces revealed higher oscillations in the magnitude and frequency of vibration with the models having lower bistability ratios. The profile shape of such models (e.g., $\overline{h} = 2$) remained symmetric with full compression under impact load. The response of the models was also characterised by infinitesimal vibrations without buckling, corresponding to the models of high $\overline{h}$.

Although higher modes of deformations were ignored in the study, the analytical models showed reasonable corroboration with the numerical models for the lattice and higher degree corroboration for the individual CDB pair. The force–time histories of the analytical and numerical FE models were consistent, and the captured peak force of the latter was 8% different from the former one on average. The response of the lattices having the lower bistability ratio was more erratic due to the residual vibrations and saddle-node bifurcations of the CDB at different layers. Small perturbations of the CDB in the lower beams occurred simultaneously with the deformation of the CDB in the upper layers, which leads to the discrepancy in the time of occurrence of the peak forces throughout the motion.

The overall response of the lattice structure made of such beams becomes more complex as relative displacements between the beams may occur which correspond to other deformation modes. It should also be emphasised that, in practice, the buckling phases are interspersed with rotations and displacements of the beams. Thus, introducing a more sophisticated model by retaining the higher modes would be at the expense of higher levels of mathematical complexity and simulation time. Such an approach would give rise to an infinitesimal improvement of the model accuracy while rendering the analyses unnecessarily complicated.

Declaration of Competing Interest

The authors declare that they have no known competing financial interests or personal relationships that could have appeared to influence the work reported in this paper.

Data availability

Data will be made available on request.

Acknowledgements

This work was supported by the University of Liverpool's Industrial Strategy Pump Priming Fund 2019/20.

Appendix

Appendix A

The parameters of Eq. (45) are given as.

$$a_2 = -14112\psi\left(\left(\frac{5p_s^5}{49}-\frac{17p_s^4}{98}+\left(-\frac{314a_1^2}{49}-\frac{5}{98}\right)p_s^3+\left(\frac{235a_1^2}{49}+\frac{25}{196}\right)p_s^2+\left(a_1^4-\frac{53}{98a_1^2}-\frac{27}{784}\right)p_s+\frac{15a_1^4}{98}-\frac{9a_1^2}{196}-\frac{1}{1568}\right)\psi+\frac{72\lambda_1\left(p_s-\frac{1}{2}\right)\left(a_1^2-\frac{1}{3p_s^2}+\frac{1}{3p_s}-\frac{1}{12}\right)\lambda_0}{49}\right) \tag{A. 52}$$

$$a_3 = 36864\psi p_s\left(\left(-\frac{20p_s^4}{3}+8p_s^3+\left(-\frac{29a_1^2}{3}-4\right)p_s^2+\left(\frac{13a_1^2}{3}+1\right)p_s+a_1^4+\frac{a_1^2}{4}-\frac{1}{12}\right)\psi+\frac{32\lambda_1\left(a_1-\frac{1}{2}+p_s\right)\lambda_0\left(a_1+\frac{1}{2}-p_s\right)}{9}\right) \tag{A. 53}$$

$$b_2 = -1440\psi a_1\left(\left(-27p_s^4+\frac{162p_s^3}{5}+\left(\frac{238a_1^2}{5}-\frac{87}{10}\right)p_s^2+\left(-\frac{74a_1^2}{5}-\frac{1}{2}\right)p_s+a_1^4-\frac{11a_1^2}{10}+\frac{1}{16}\right)\psi-\frac{24\lambda_1\lambda_0\left(a_1^2-3p_s^2+3p_s-\frac{3}{4}\right)}{5}\right) \tag{A. 54}$$

$$a_4 = -480\left(p_s-\frac{1}{2}\right)\psi^2\left(\frac{p_s^4}{5}-\frac{2p_s^3}{5}+\left(-2a_1^2+\frac{3}{10}\right)p_s^2+\left(2a_1^2-\frac{1}{10}\right)p_s+a_1^4-\frac{a_1^2}{2}+\frac{1}{80}\right) \tag{A. 55}$$

$$a_5 = 3072\psi^2 p_s\left(-p_s^2+(-2a_1+1)p_s+a_1^2+a_1-\frac{1}{4}\right)\left(-p_s^2+(2a_1+1)p_s+a_1^2-a_1-\frac{1}{4}\right) \tag{A. 56}$$

$$b_3 = 96\psi^2\left(5p_s^4-10p_s^3+\left(-10a_1^2+\frac{15}{2}\right)p_s^2+\left(10a_1^2-\frac{5}{2}\right)p_s+a_1^4-\frac{5a_1^2}{2}+\frac{5}{16}\right)a_1 \tag{A. 57}$$

$$b_4 = 270336\psi p_s a_1\left(\left(\frac{5p_s^3}{11}-\frac{7p_s^2}{22}+\left(a_1^2+\frac{1}{4}\right)p_s-\frac{3a_1^2}{22}-\frac{5}{88}\right)\psi+\frac{32\lambda_1\left(p_s-\frac{1}{2}\right)\lambda_0}{33}\right) \tag{A. 58}$$

$$a_6 = \Big(\big(-593280p_s^5 + 596160p_s^4 + \big(-403200a_1^2 - 258048 \big) p_s^3 + \big(150912a_1^2 + 52416 \big) p_s^2 + \big(-31104a_1^4 - 17280a_1^2 - 3816 \big) p_s - 2880a_1^4 + 576a_1^2 + 36 \big) \psi^2 - 9216\lambda_0\lambda_1 \Big(-\frac{65p_s^3}{6} + \frac{67p_s^2}{12} + \Big(-\frac{61a_1^2}{6} - \frac{35}{24} \Big) p_s - \frac{a1^2}{4} + \frac{1}{48} \Big) \psi + 98304\lambda_0^2 \Big(\Big(-\frac{\lambda_0\lambda_2}{2} - \frac{\lambda_1^2}{4} \Big) p_s + \frac{\lambda_0\lambda_2}{4} + \frac{\lambda_1^2}{8} \Big) \Big) \tag{A. 59}$$

$$b_6 = \Big(-7680 \Big(-\frac{373p_s^4}{5} + \frac{719p_s^3}{20} + \Big(-\frac{716}{5}a_1^2 - \frac{1843}{80} \Big) p_s^2 + \Big(\frac{387a_1^2}{20} + \frac{163}{40} \Big) p_s + a_1^4 - \frac{11a_1^2}{80} - \frac{7}{64} \Big) a_1\psi^2 - 11520\lambda_1\lambda_0 a_1 \Big(a_1^2 - \frac{2951}{45p_s^2} + \frac{1543}{45p_s} - \frac{3}{4} \Big) \psi - 98304\lambda_0^2 \Big(-\lambda_0\lambda_2 - \frac{\lambda_1^2}{2} \Big) a_1 \Big) \tag{A. 60}$$

$$b_5 = 12288 \Big(p_s - \frac{1}{2} \Big) \psi^2 \Big(a_1 - \frac{1}{2} + p_s \Big) p_s \Big(a1 + \frac{1}{2} - p_s \Big) a_1 \tag{A. 61}$$

References

Al Kassem, G., Weichert, D., 2010. Micromechanical material models for polymer composites through advanced numerical simulation techniques. publication server of RWTH Aachen University, Aachen.

Alderson, A., Alderson, K.L., 2007. Auxetic materials. Proc. Inst. Mech. Eng. Part G J. Aerosp. Eng. 221 (4), 565–575. https://doi.org/10.1243/09544100JAERO185.

Alonso-Mora, J., Naegeli, T., Siegwart, R., Beardsley, P., 2015. Collision avoidance for aerial vehicles in multi-agent scenarios. Auton. Robots 39 (1), 101–121. https://doi.org/10.1007/s10514-015-9429-0.

Baughman, R.H., 2003. Auxetic materials: Avoiding the shrink. Nature 425 (6959), 667. https://doi.org/10.1038/425667a.

Bazant, P.Z., Cedolin, L., 2010. Stability of Structures, 4th ed. World Scientific Publishing Co., Pte. Ltd, London.

Bouaoune, L., Brunet, Y., El Moumen, A., Kanit, T., Mazouz, H., 2016. Random versus periodic microstructures for elasticity of fibers reinforced composites. Compos. Part B Eng. 103, 68–73. https://doi.org/10.1016/j.compositesb.2016.08.026.

Brunet, T., Merlin, A., Mascaro, B., Zimny, K., Leng, J., Poncelet, O., Aristégui, C., Mondain-Monval, O., 2015. Soft 3D acoustic metamaterial with negative index. Nat. Mater. 14 (4), 384–388.

Camescasse, B., Fernandes, A., Pouget, J., 2013. Bistable buckled beam: Elastica modeling and analysis of static actuation. Int. J. Solids Struct. 50 (19), 2881–2893. https://doi.org/10.1016/j.ijsolstr.2013.05.005.

Cazottes, P., Fernandes, A., Pouget, J., Hafez, M., 2009. Bistable buckled beam: Modeling of actuating force and experimental validations. J. Mech. Des. Trans. ASME 131 (10), 1010011–10100110. https://doi.org/10.1115/1.3179003.

Chen, S., et al., 2019. A novel composite negative stiffness structure for recoverable trapping energy. Compos. Part A Appl. Sci. Manuf. 129 (November), 105697. https://doi.org/10.1016/j.compositesa.2019.105697.

Chen, Y., Jin, L., 2020. Snapping-back buckling of wide hyperelastic columns. Extrem. Mech. Lett. 34 (November), 100600 https://doi.org/10.1016/j.eml.2019.100600.

Dassault Systèmes Simulia Corp., "Shell Elements in ABAQUS / Explicit Conventional Shell Elements," *Ind. Present. Softw. Prop.*, 2005, [Online]. Available: http://imechanica.org/files/appendix2-shells_2.pdf.

Correa, D.M., Seepersad, C.C., Haberman, M.R., 2015. Mechanical design of negative stiffness honeycomb materials. Integr. Mater. Manuf. Innov. 4 (1), 165–175. https://doi.org/10.1186/s40192-015-0038-8.

Chen, Y., Lu, C., Yan, J., Feng, J., Sareh, P., 2022. Intelligent computational design of scalene-faceted flat-foldable tessellations. Journal of Computational Design and Engineering 9 (5), 1765–1774.

Chen, Y., Shi, J., He, R., Lu, C., Shi, P., Feng, J., Sareh, P., 2023. A unified inverse design and optimization workflow for the Miura-oRing metastructure. Journal of Mechanical Design 1–34.

Chen, Y., Xu, R., Lu, C., Liu, K., Feng, J., Sareh, P., 2023. Multi-stability of the hexagonal origami hypar based on group theory and symmetry breaking. International Journal of Mechanical Sciences 247, 108196.

Chen, Y., Yan, J., Feng, J., Sareh, P., 2021. Particle swarm optimization-based metaheuristic design generation of non-trivial flat-foldable origami tessellations with degree-4 vertices. Journal of Mechanical Design 143 (1).

Chen, Y., Ye, W., Xu, R., Sun, Y., Feng, J., Sareh, P., 2023. A programmable auxetic metamaterial with tunable crystal symmetry. International Journal of Mechanical Sciences 249, 108249.

Correa, D.M., Klatt, T., Cortes, S., Haberman, M., Kovar, D., Seepersad, C., 2015. Negative stiffness honeycombs for recoverable shock isolation. Rapid Prototyp. J. 21 (2), 193–200. https://doi.org/10.1108/RPJ-12-2014-0182.

Daynes, S., Potter, K.D., Weaver, P.M., 2008. Bistable prestressed buckled laminates. Compos. Sci. Technol. 68 (15–16), 3431–3437. https://doi.org/10.1016/j.compscitech.2008.09.036.

Dean, J., A. S-Fallah, P. M. Brown, L. A. Louca, and T. W. Clyne,, 2011. Energy absorption during projectile perforation of lightweight sandwich panels with metallic fibre cores. Compos. Struct. 93 (3), 1089–1095. https://doi.org/10.1016/j.compstruct.2010.09.019.

Emam, S.A., 2002. "A Theoretical and Experimental Study of Nonlinear Dynamics of Buckled Beams. Virginia Polytechnic Institute and State University. PhD Thesis",.

Fallah, A.S., Yang, Y., Ward, R., Tootkaboni, M., Brambleby, R., Louhghalam, A., Louca, L.A., 2015. Wave propagation in two-dimensional anisotropic acoustic metamaterials of K4 topology. Wave Motion 58, 101–116.

Fang, N., Xi, D., Xu, J., Ambati, M., Srituravanich, W., Sun, C., Zhang, X., 2006. Ultrasonic metamaterials with negative modulus. Nat. Mater. 5 (6), 452–456.

Feldgun, V.R., Yankelevsky, D.Z., Karinski, Y.S., 2016. A nonlinear SDOF model for blast response simulation of elastic thin rectangular plates. Int. J. Impact Eng. 88, 172–188. https://doi.org/10.1016/j.ijimpeng.2015.09.001.

Frenzel, T., Kadic, M., Wegener, M., 2017. Three-dimensional mechanical metamaterials with a twist. Science (80-.) 358 (6366), 1072–1074. https://doi.org/10.1126/science.aao4640.

Fulcher, B.A., Shahan, D.W., Haberman, M.R., Seepersad, C.C., Wilson, P.S., 2014. Analytical and experimental investigation of buckled beams as negative stiffness elements for passive vibration and shock isolation systems. J. Vib. Acoust. Trans. ASME 136 (3), 1–12. https://doi.org/10.1115/1.4026888.

Garoz, D., Gilabert, F.A., Sevenois, R.D.B., Spronk, S.W.F., Van Paepegem, W., 2019. Consistent application of periodic boundary conditions in implicit and explicit finite element simulations of damage in composites. Comp. Part B: Eng. 168, 254–266.

Gibson, L., Ashby, M.F., 1997. Cellular solids, 2nd ed. Cambridge University Press.

Gibson, L.J., Ashby, M.F., 2001. *Cellular Solids Structure and porperties*, Second. Cambridge University Press, Cambridge.

Goldsberry, B.M., Haberman, M.R., 2018. Negative stiffness honeycombs as tunable elastic metamaterials. J. Appl. Phys. 123 (9), pp. https://doi.org/10.1063/1.5011400.

Gorshkov, V.N., Bereznykov, O.V., Boiger, G.K., Sareh, P., Fallah, A.S., 2023. Acoustic metamaterials with controllable bandgap gates based on magnetorheological elastomers. International Journal of Mechanical Sciences 238, 107829.

Gorshkov, V.N., Navadeh, N., Sareh, P., Tereshchuk, V.V., Fallah, A.S., 2017. Sonic metamaterials: Reflection on the role of topology on dispersion surface morphology. Mater. Des. 132 (June), 44–56. https://doi.org/10.1016/j.matdes.2017.06.049.

Gorshkov, V., Sareh, P., Navadeh, N., Tereshchuk, V., Fallah, A.S., 2021. Multi-resonator metamaterials as multi-band metastructures. Materials & Design 202, 109522.

Hou, B., Pattofatto, S., Li, Y.L., Zhao, H., 2011. Impact behavior of honeycombs under combined shear-compression. Part II: Analysis. Int. J. Solids Struct. 48 (5), 687–697. https://doi.org/10.1016/j.ijsolstr.2010.11.005.

Hou, B., Zhao, H., Pattofatto, S., Liu, J.G., Li, Y.L., 2012. Inertia effects on the progressive crushing of aluminium honeycombs under impact loading. Int. J. Solids Struct. 49 (19–20), 2754–2762. https://doi.org/10.1016/j.ijsolstr.2012.05.005.

Hu, L., You, F., Yu, T., 2013. Effect of cell-wall angle on the in-plane crushing behaviour of hexagonal honeycombs. Mater. Des. 46 (November), 511–523. https://doi.org/10.1016/j.matdes.2012.10.050.

Hu, L.L., Yu, T.X., 2010. Dynamic crushing strength of hexagonal honeycombs. Int. J. Impact Eng. 37 (5), 467–474. https://doi.org/10.1016/j.ijimpeng.2009.12.001.

Hu, L.L., Yu, T.X., 2013. Mechanical behavior of hexagonal honeycombs under low-velocity impact - Theory and simulations. Int. J. Solids Struct. 50 (20–21), 3152–3165. https://doi.org/10.1016/j.ijsolstr.2013.05.017.

Hu, L.L., Zhou, M.Z., Deng, H., 2018. Dynamic crushing response of auxetic honeycombs under large deformation: Theoretical analysis and numerical simulation. Thin-Walled Struct. 131 (July), 373–384. https://doi.org/10.1016/j.tws.2018.04.020.

Jalali, E., Soltanizadeh, H., Chen, Y., Xie, Y.M., Sareh, P., 2022. Selective hinge removal strategy for architecting hierarchical auxetic metamaterials. Communications Materials 3 (1), 97.

Jeong, H.Y., Lee, E., Ha, S., Kim, N., Jun, Y.C., 2019. Multistable Thermal Actuators Via Multimaterial 4D Printing. Adv. Mater. Technol. 4 (3), 1–7. https://doi.org/10.1002/admt.201800495.

Johnson, H.E., Louca, L.A., Mouring, S., Fallah, A.S., 2009. Modelling impact damage in marine composite panels. Int. J. Impact Eng. 36 (1), 25–39. https://doi.org/10.1016/j.ijimpeng.2008.01.013.

Jones, N., 1971. A theoretical study of the dynamic plastic behaviour of beams and plates with finite-deflections. Int. J. Solids Struct. 7 (33), 1007–1029.

Jones, N., 1989. Structural Impact. Cambridge University Press, Cambridge.

Jones, N., 2012. Impact loading of ductile rectangular plates. Thin-Walled Struct. 50 (1), 68–75. https://doi.org/10.1016/j.tws.2011.09.006.
Jones, N., 2014. Dynamic inelastic response of strain rate sensitive ductile plates due to large impact, dynamic pressure and explosive loadings. Int. J. Impact Eng. 74, 3–15. https://doi.org/10.1016/j.ijimpeng.2013.05.003.
Jones, N., 2014. Pseudo-shakedown phenomenon for the mass impact loading of plating. Int. J. Impact Eng. 65, 33–39. https://doi.org/10.1016/j.ijimpeng.2013.10.009.
Jones, N., Walters, R., 1983. Large deflections of rectangular plates. J. Sh. Res. 18 (2), 125–131. https://doi.org/10.1016/0020-7462(83)90040-9.
Kochmann, D.M., Bertoldi, K., 2017. Exploiting Microstructural Instabilities in Solids and Structures: From Metamaterials to Structural Transitions. Appl. Mech. Rev. 69 (5), Oct. https://doi.org/10.1115/1.4037966.
Konarski, S.G., Haberman, M.R., Hamilton, M.F., 2020. Acoustic response for nonlinear, coupled multiscale model containing subwavelength designed microstructure instabilities. Phys. Rev. E 101 (2), 1–12. https://doi.org/10.1103/PhysRevE.101.022215.
Lakes, R., 2001. Elastic and viscoelastic behavior of chiral materials. Int. J. Mech. Sci. 43 (7), 1579–1589. https://doi.org/10.1016/S0020-7403(00)00100-4.
Lakes, R.S., Lee, T., Bersie, A., Wang, Y.C., 2001. Extreme damping in composite materials with negative-stiffness inclusions. Nature 410 (6828), 565–567. https://doi.org/10.1038/35069035.
Li, Q.M., Jones, N., 2000. On dimensionless numbers for dynamic plastic response of structural members. Arch. Appl. Mech. 70 (4), 245–254. https://doi.org/10.1007/s004199900072.
Li, S.R., Teng, Z.C., Zhou, Y.H., 2004. Free vibration of heated Euler-Bernoulli beams with thermal postbuckling deformations. J. Therm. Stress. 27 (9), 843–856. https://doi.org/10.1080/01495730490486352.
Liu, K., Tachi, T., Paulino, G.H., 2019. Invariant and smooth limit of discrete geometry folded from bistable origami leading to multistable metasurfaces. Nat. Commun. 10 (1), 1–10. https://doi.org/10.1038/s41467-019-11935-x.
Lu, C., Chen, Y., Yan, J., Feng, J., Sareh, P., 2024. Algorithmic spatial form-finding of four-fold origami structures based on mountain-valley assignments. Journal of Mechanisms and Robotics 16 (3), 031001.
Lv, C., Krishnaraju, D., Konjevod, G., Yu, H., Jiang, H., 2014. Origami based mechanical metamaterials. Sci. Rep. 4 https://doi.org/10.1038/srep05979.
Ma, G., Sheng, P., 2016. Acoustic metamaterials: From local resonances to broad horizons. Sci. Adv. 2 (2).
Meaud, J., 2018. Multistable two-dimensional spring-mass lattices with tunable band gaps and wave directionality. J. Sound Vib. 434, 44–62. https://doi.org/10.1016/j.jsv.2018.07.032.
Mehreganian, N., Fallah, A.S.S., Louca, L.A.A., 2018. Dynamic Performance of Simply Supported Rigid-Plastic Square Plates Subject to Localized Blast Loading. J. Eng. Mech. 140 (1), 159–171. https://doi.org/10.1061/(ASCE)EM.1943-7889.0000645.
Mehreganian, N., Fallah, A.S., Louca, L.A., 2018. Inelastic dynamic response of square membranes subjected to localised blast loading. Int. J. Mech. Sci. 148 (November), 578–595. https://doi.org/10.1016/j.ijmecsci.2018.09.017.
Mehreganian, N., Fallah, A.S., Louca, L.A., 2019. Nonlinear dynamics of locally pulse loaded square Föppl–von Kármán thin plates. International Journal of Mechanical Sciences 163, 105157.
Mehreganian, N., Fallah, A.S., Sareh, P., 2021. Structural Mechanics of Negative Stiffness Honeycomb Metamaterials. J. Appl. Mech. 88 (May), 1–18. https://doi.org/10.1115/1.4049954.
Mehreganian, N., Toolabi, M., Zhuk, Y.A., Etminan Moghadam, F., Louca, L.A., Fallah, A. S., 2021. Dynamics of pulse-loaded circular Föppl-von Kármán thin plates-Analytical and numerical studies. J. Sound Vib. 513, 116413 https://doi.org/10.1016/j.jsv.2021.116413.
Mooney, J.G., Johnson, E.N., 2013. A Collision-resilient Flying Robot. J. F. Robot. 31 (4), 496–509. https://doi.org/10.1002/rob.21495.
Nayfeh, A.H., Emam, S.A., 2008. Exact solution and stability of postbuckling configurations of beams. Nonlinear Dyn. 54 (4), 395–408. https://doi.org/10.1007/s11071-008-9338-2.
Okumura, D., Ohno, N., Noguchi, C., 2002. Post-buckling analysis of elastic honeycombs subject to in-plane biaxial compression. Int. J. Solids Struct. Sci. 39 (13–14), 3487–3503. https://doi.org/10.1016/S0020-7683(02)00165-8.
Ouyang, S., Deng, Z., Hou, X., 2018. Stress concentration in octagonal honeycombs due to defects. Compos. Struct. 204 (March), 814–821. https://doi.org/10.1016/j.compstruct.2018.07.087.
Qiu, J., 2003. An Electrothermally-Actuated Bistable MEMS Relay for Power Applications. Massachusetts Institute of Technology.
Qiu, J., Lang, J.H., Slocum, A.H., 2004. A curved-beam bistable mechanism. J. Microelectromechanical Syst. 13 (2), 137–146. https://doi.org/10.1109/JMEMS.2004.825308.
Rafsanjani, A., Akbarzadeh, A., Pasini, D., 2015. Snapping Mechanical Metamaterials under Tension. Adv. Mater. 27 (39), 5931–5935. https://doi.org/10.1002/adma.201502809.
Restrepo, D., Mankame, N.D., Zavattieri, P.D., 2015. Phase transforming cellular materials. Extrem. Mech. Lett. 4 (September), 52–60. https://doi.org/10.1016/j.eml.2015.08.001.
Sareh, P., 2019. The least symmetric crystallographic derivative of the developable double corrugation surface: Computational design using underlying conic and cubic curves. Mater. Des. 183, 108128 https://doi.org/10.1016/j.matdes.2019.108128.
Sareh, P., Chermprayong, P., Emmanuelli, M., Nadeem, H., Kovac, M., 2018. Rotorigami: A rotary origami protective system for robotic rotorcraft. Sci. Robot. 3 (22), 1–13. https://doi.org/10.1126/scirobotics.aah5228.
Sareh, P., Guest, S.D., 2014. Designing symmetric derivatives of the Miura-ori. In: *Advances in Architectural Geometry 2014*. Springer International Publishing, Cham, pp. 233–241.
Sareh, P., Guest, S.D., 2015. Design of isomorphic symmetric descendants of the Miura-ori. Smart Materials and Structures 24 (8), 085001.
Sareh, P., Guest, S.D., 2015. Design of non-isomorphic symmetric descendants of the Miura-ori. Smart Materials and Structures 24 (8), 085002.Chicago.
Sareh, P., Guest, S.D., 2015. A framework for the symmetric generalisation of the Miura-ori. International Journal of Space Structures 30 (2), 141–152.
Shan, S., et al., 2015. Multistable architected materials for trapping elastic strain energy. Adv. Mater. 27 (29), 4296–4301. https://doi.org/10.1002/adma.201501708.
Street, T., Seffen, K.A., 2007. 'Morphing' bistable orthotropic elliptical shallow shells. Proc. R. Soc. A Math. Phys. Eng. Sci. 463 (2077), 67–83. https://doi.org/10.1098/rspa.2006.1750.
Sun, S., An, N., Wang, G., Li, M., Zhou, J., 2019. Snap-back induced hysteresis in an elastic mechanical metamaterial under tension. Appl. Phys. Lett. 115 (9), pp. https://doi.org/10.1063/1.5119275.
R. Szilard, *Theories and Applications of Plate Analysis*. 2004.
Tancogne-Dejean, T., Spierings, A.B., Mohr, D., 2016. Additively-manufactured metallic micro-lattice materials for high specific energy absorption under static and dynamic loading. Acta Mater. 116 (June), 14–28. https://doi.org/10.1016/j.actamat.2016.05.054.
Tian, W., Qi, L., Chao, X., Liang, J., Fu, M., 2019. Periodic boundary condition and its numerical implementation algorithm for the evaluation of effective mechanical properties of the composites with complicated micro-structures. Compos. Part B 162 (June 2018), 1–10. https://doi.org/10.1016/j.compositesb.2018.10.053.
Toupin, R., 2013. Elastic materials with couple-stresses To cite this version : HAL Id : hal-00852443. Arch. Ration. Mech. Anal. 11 (1), 385–414.
Truesdell, C., 1968. The Elements of Continuum Mechanics. Springer, Berlin Heidelberg NewYork. January.
C. Truesdell and R. Toupin, "The Classical Field Theories," in *Principles of Classical Mechanics and Field Theory / Prinzipien der Klassischen Mechanik und Feldtheorie*, S. Flügge, Ed. Berlin, Heidelberg: Springer Berlin Heidelberg, 1960, pp. 226–858.
Vangbo, M., 1998. An analytical analysis of a compressed bistable buckled beam. Sensors Actuators, A Phys. 69 (3), 212–216. https://doi.org/10.1016/S0924-4247(98)00097-1.
Wadee, M.A., Hadjipantelis, N., Bazzano, J.B., Gardner, L., Lozano-Galant, J.A., 2020. Stability of steel struts with externally anchored prestressed cables. J. Constr. Steel Res. 164, 105790 https://doi.org/10.1016/j.jcsr.2019.105790.
Wu, W., Hu, W., Qian, G., Liao, H., Xu, X., Berto, F., 2019. Mechanical design and multifunctional applications of chiral mechanical metamaterials: A review. Mater. Des. vol. 180, no. June, 107950 https://doi.org/10.1016/j.matdes.2019.107950.
Yavari, A., 2008. On geometric discretization of elasticity. J. Math. Phys. 49 (2), 1–36. https://doi.org/10.1063/1.2830977.
Yavari, A., Sarkani, S., Moyer, E.T., 2000. On applications of generalized functions to beam bending problems. Int. J. Solids Struct. 37 (40), 5675–5705. https://doi.org/10.1016/S0020-7683(99)00271-1.
Zheng, X., Guo, X., Watanabe, I., 2021. A mathematically defined 3D auxetic metamaterial with tunable mechanical and conduction properties. Mater. Des. 198, 109313 https://doi.org/10.1016/j.matdes.2020.109313.
Zheng, Z., Yu, J., Li, J., 2005. Dynamic crushing of 2D cellular structures: A finite element study. Int. J. Impact Eng. 32 (1–4), 650–664. https://doi.org/10.1016/j.ijimpeng.2005.05.007.
Zou, Z., Reid, S.R., Tan, P.J., Li, S., Harrigan, J.J., 2009. Dynamic crushing of honeycombs and features of shock fronts. Int. J. Impact Eng. 36 (1), 165–176. https://doi.org/10.1016/j.ijimpeng.2007.11.008.